Title
Computational and Experimental Study of Hemodynamics in Abdominal Aortic Aneurysms

Permalink
https://escholarship.org/uc/item/03k6c83q

Author
Surianarayanan, Nishanth

Publication Date
2020

Peer reviewed|Thesis/dissertation

UNIVERSITY OF CALIFORNIA SAN DIEGO

Computational and Experimental Study of Hemodynamics in Abdominal Aortic Aneurysms

A Thesis submitted in partial satisfaction of the
requirements for the degree
Master of Science

in

Engineering Sciences with a Specialization in Mechanical Engineering

by

Nishanth Surianarayanan

Committee in charge:

Professor Juan Lasheras, Chair
Professor Andrew Barleben, Co-Chair
Professor Abhishek Saha

2020

The Thesis of Nishanth Surianarayanan is approved, and it is acceptable in quality and form for publication on microfilm and electronically:

Co-Chair

Chair

University of California San Diego

2020

Table of Contents

List of Figures

List of Tables

ABSTRACT OF THE THESIS

Computational and Experimental Study of Hemodynamics in Abdominal Aortic Aneurysms

by

Nishanth Surianarayanan
Master of Science in Mechanical and Aerospace Engineering
University of California San Diego, 2020

Professor Juan Lasheras, Chair
Professor Andrew Barleben, Co-Chair

An abdominal aortic aneurysm (AAA) is a localized dilation of the abdominal aorta resulting from the weakening of the aorta wall. Most of the human AAA's harbor an intraluminal thrombus. However, its role in AAA progression is unclear and hence, it is important to understand the role of hemodynamics in thrombus formation. A detailed literature survey on phantom fabrication, in-vitro flow loop setup, and CFD studies indicated that intense research activity is pursued currently to evolve strategies for better diagnosis and surgical interventions. In this thesis work, a procedure for aneurysm phantom fabrication was standardized and experimentally demonstrated by adopting a 2-axis rotation coating method. Further, an in-vitro mock circulatory flow loop was designed and tested. Through image-based computational fluid dynamics studies, the reason for thrombus initiation and deposition was explored through the study of near-wall quantities such as time-averaged wall shear stress, oscillatory shear index, endothelial cell activation potential, and residence time. The various hemodynamic quantities well-predicted the region of thrombus initiation and deposition due to the high residence time and hot spots of Endothelial Cell Activation Potential observed in the actual site of thrombus deposition in the patient.

Chapter 1

Abdominal Aortic Aneurysms

1.1 Introduction

Abdominal aortic aneurysm (AAA) is a localized dilation greater than 3 cm of the abdominal aorta resulting from the weakening of the aorta wall (Humphrey et al. 2008). AAA is the 14th leading leading cause of death in the United States with 10,000 deaths annually (Benjamin EJ et al. 2018). The main complication of a AAA is aneurysm rupture, which happens when the wall cannot withstand the stresses from the blood flow. The most difficult aspect is the diagnosis as AAAs remain asymptomatic until rupture and may only be detected during incidental examination. The risk factors include tobacco use, age (in people aged 65 or older), high blood pressure, male gender, family history and presence of other aneurysms (Lasheras 2007). The formation of AAA is attributed to the complex interplay of biological and hemodynamic factors. On the cellular scale, AAAs are believed to form due to chronic inflammation, which causes the release of proteolytic enzymes, such as Matrix metalloproteinase (MMP), Cysteine proteases, oxidation-derived free redicals and cytokines (Golledge 2019). These enzymes lead to the destruction of aortic media and vascular smooth muscle cells (SMC) apoptosis and dysfunction, which initiates the formation of AAAs.

Another theory suggests that atherosclerosis leads to AAA formation. According to this theory, the abdominal aortic aneurysm expands in total cross-section in response to atherosclerotic plague growth, to maintain lumen dimension. This positive remodelling process may become excessive, leading to the formation of AAAs. It is also believed that hemodynamic forces such as wall shear stresses and strain initiates inflammation or atherosclerosis, which in turn leads to AAA formation (Golledge 2019). Most of the human AAAs harbour intraluminal thrombus (ILT), however, its role in AAA progression and rupture remains unclear. Some studies suggest that ILT causes hypoxia of AAA wall, leading to degradation and subsequent wall weakening (Lasheras 2007). Some other studies have shown that ILT reduces wall shear stresses, which limits AAA growth and rupture (Speelman et al. 2010).

1.2 AAA Treatment Options

Before the 1990s, the only treatment option for an abdominal aortic aneurysm was an open repair. In an open repair, the abdominal aortic aneurysm is accessed through a midline laparotomy. The aorta is cross-clamped at the infrarenal and iliacs to isolate the aneurysm region from blood flow. The aneurysm is dissected and the intraluminal thrombus is removed. A synthetic graft is sutured to the proximal and distal ends to replace the aneurysm segment and finally, the aneurysm sac is sutured around the graft. This open repair is associated with a high mortality rate of % and was often not suitable for older patients with comorbidities.

During the 1990s, a minimally invasive treatment option developed, known as the Endovascular Aneurysm Repair (EVAR). Through this technique, a stent-graft was positioned in the aneurysm through the femoral artery, to bypass the aneurysm section and prevent blood forces on the aneurysm wall. A successful EVAR depends on sufficient proximal and distal sealing. The EVAR is associated with reduced mortality compared to Open repair due to its minimally invasive nature and enabled treatment for older people who were unsuitable for open repair. However, on the long term, EVAR was associated with higher complications than the open repair. Thus, the open repair is often recommended for younger patients, people with no or fewer comorbidities and for patients whose complex anatomy prevents the proper fixation of a stent-graft. On the other hand, EVAR is recommended for older patients, patients with significant comorbidities and for patients with prior aortic and abdominal surgeries (Swerdlow et al. 2019).

1.3 Endoleaks: A Complication of EVAR

There are several complications of the EVAR procedure, such as stent-graft migration, stent-graft infection and endoleaks. However, we limit our discussion to only Endoleaks, a major and frequent complication of EVAR. Endoleaks refers to blood flow in the aneurysm post the placement of a stent-graft due to leaks from inadequate proximal and distal sealing of stent-graft (Type I endoleak), due to backflow from arteries emerging in the abdominal aorta section (Type II endoleak), due to disconnection of stent-graft components (Type III endoleak), inherent graft defects (Type IV endoleak), and aneurysm expansion due to unidentifiable leaks (Type IV endoleak). Out of the different types, Type II endoleak is the most common endoleak type, occurring due to backflow from the lumbar arteries or the inferior mesenteric artery. The type II endoleak occurs commonly after EVAR procedure and about 1/3rd of them resolve automatically (Swerdlow et al. 2019). Thus, intervention is performed only when sac expansion is observed. Generally, a transarterial, translumbar or transcaval approach is adopted to embolize the backbleeding artery.

1.4 Objective of Entire Project

a) Using detailed patient-specific anatomy, identify high-risk patients for late failure due to endoleaks and subsequent graft failure.

b) Identify the critical flaws in EVAR aneurysm repair in high-risk patients.

1.5 Steps in Entire Project

The following are the steps involved in the experimental part of the project:

a) Develop a reliable and consistent method for model fabrication.

b) Devise setup for in-vitro experiments.

c) Setup the particle image velocimetry system with appropriate lens, laser and camera, and conduct measurements in a simple model to get reliable PIV results.

d) Fabricate final model and perform PIV measurements with and without stent-graft.

The following are the steps involved in the computational part of the project:

a) Perform CFD simulations in the patient prior to endovascular aneurysm repair in aneurysm lumen geometry as well as in the aneurysm wall geometry to study hemodynamics within the aneurysm.

b) Incorporate stent-graft inside computational domain to study type II endoleaks.

1.6 Thesis Scope and Outline

This study includes development of a patient-specific silicone model fabrication protocol, construction of the in-vitro flow loop setup and computational studies in the aneurysm lumen and aneurysm wall geometry to establish the hemodynamic reasons for the observed thrombus formation in the patient based on parameters such as time-averaged wall shear stress, oscillatory shear index and endothelial cell activation potential and residence time.

Bibliography

[1] Benjamin, E. J., Virani, S. S., Callaway, C. W., Chamberlain, A. M., Chang, A. R., Cheng, S., Chiuve, S. E., Cushman, M., Delling, F. N., Deo, R., de Ferranti, S. D., Ferguson, J. F., Fornage, M., Gillespie, C., Isasi, C. R., Jiménez, M. C., Jordan, L. C., Judd, S. E., Lackland, D., Lichtman, J. H., Lisabeth, L., Liu, S., Longenecker, C. T., Lutsey, P. L., Mackey, J. S., Matchar, D. B., Matsushita, K., Mussolino, M. E., Nasir, K., O'Flaherty, M., Palaniappan, L. P., Pandey, A., Pandey, D. K., Reeves, M. J., Ritchey, M. D., Rodriguez, C. J., Roth, G. A., Rosamond, W. D., Sampson, U. K. A., Satou, G. M., Shah, S. H., Spartano, N. L., Tirschwell, D. L., Tsao, C. W., Voeks, J. H., Willey, J. Z., Wilkins, J. T., Wu, J. H., Alger, H. M., Wong, S. S. & Muntner, P. American Heart Association Council on Epidemiology and Prevention Statistics Committee and Stroke Statistics Subcommittee; American Heart Association Council on Epidemiology and Prevention Statistics Committee and Stroke Statistics Subcommittee. Heart disease and stroke statistics-2018 update: a report from the American Heart Association. *Circulation* **137**, e67– e492 (2018).

[2] Golledge, J. Abdominal aortic aneurysm: update on pathogenesis and medical treatments. *Nature Reviews Cardiology* **16**, 225–242 (2019).

[3] Humphrey, J. D. & Taylor, C. A. Intracranial and Abdominal Aortic Aneurysms: Similarities, Differences, and Need for a New Class of Computational Models. *Annual Review of Biomedical Engineering* **10**, 221–246 (2008).

[4] Lasheras, J. C. The Biomechanics of Arterial Aneurysms. *Annual Review of Fluid Mechanics* **39**, 293–319 (2007).

[5] Speelman, L., Schurink, G., Bosboom, E., Buth, J., Breeuwer, M., van de Vosse, F. & Jacobs, M. The mechanical role of thrombus on the growth rate of an abdominal aortic aneurysm. *Journal of Vascular Surgery* **51**, 19-26 (2010).

[6] Swerdlow, N. J., Wu, W. W. & Schermerhorn, M. L. Open and Endovascular Management of Aortic Aneurysms. *Circulation research* **124**, 647–661 (2019).

Chapter 2

In-vitro Phantom Fabrication

2.1 Model Fabrication

Anatomically accurate models of the cardiovascular system is used in a diverse range of research and developmental applications, viz. for the estimation of 3D blood flow patterns to evaluate cardiovascular implants and for training for different clinical and surgical interventions (Karina Arcaute et al., 2008). In this chapter, the reconstruction of a patient specific abdominal aortic aneurysm complaint phantom is experimentally demonstrated and a detailed procedure is described. The merits and demerits of the chosen method is also briefly discussed.

2.2 A Review of Past Studies

The review article by Yazdi et al. (2018) comprehensively discusses the different methods of fabricating rigid and compliant models and its accuracy for experimental flow system studies. The authors provide a comparison of influential phantom fabrication methodologies, its relative benefits, costs of geometric reconstruction, and its limitations. The review concludes that high accuracy in vitro experimental simulation of hemodynamics is rather difficult with the existing manufacturing and imaging techniques. Hemodynamic modelling appears to be promising for cardiovascular treatment and its required interventions. The review covers three decades of publications (1982-2019) with 186 references.

Karina et al. (2008) employed dip-rotation coating method for manufacturing patient specific phantoms of complex geometries such as nonuniform radial geometry, tapered diameters, bifurcations and small branches. In order to provide a uniform coats, the two improvements that the authors made in the compliant phantom fabrication were the use of a low viscosity (1500 -2000 cP) silicone solution and a two axis rotation mechanism. Vertical and horizontal dipping was compared and vertical dipping was recommended for ease and fewer defects in the model. The demerits were that the fabricated silicone vessels had variable wall thicknesses.

Hütter et al. (2016) described a core-shell approach for fabricating compliant thin walled silicone phantom of the human ascending aorta and brachiocephalic artery. The authors used SolidWorks for constructing the model geometry and then 3D printed the core in Acrylonitrile butadiene styrene (ABS). The external mold was produced by CNC machining in Ebalta S-model board. 3D scanner technology was used for scanning the internal and external mold for comparing with computer model for error estimation. Although the final model did not have air bubbles, the final model had a rough external surface and did not have a consistent and desired wall thickness. The final model was not suitable for PIV imaging.

Six transparent rigid patient-specific models of intracranial aneurysms were successfully constructed by Chivukula et al. (March 2019) from three-dimensional rotational angiography imaging of patients in multiple steps. The authors claim that they could construct dimensionally accurate phantoms for in vitro studies of hemodynamics, verified with the help of high fidelity synchrotron X-ray microtomography. The study facilitated optimization of patient treatment strategies.

Fabrication of complaint patient specific models is expensive and time consuming. Ruedinger et al. (2019) successfully attempted to reconstruct low cost phantoms (Cost of one 10 cm x 10 cm x 5 cm phantom is $69) for PIV experiments. The authors used the lost-core casting technique to manufacture the phantoms. Unlike other works that involved fabricating a mold using 3D-printed replica, which were in turn used to produce the cores using materials such as wax or low-melting point alloys, the authors 3D-printed the cores directly with Polyvinyl alcohol (PVA), and used 80:20 water glue mixture for smoothing the surface. The smoothed core was encapsulated by means of Sylgard 184 and Solaris ,and the PVA was dissolved away in water to produce a silicone block with the lumen geometry. This approach is faster as the cores are 3D-printed directly, thus saving time needed for fabricating the mold. The geometric accuracy of the model was validated by computed tomography. Watts et al. (2007) also used the lost-core casting technique to fabricate carotid bifurcation lumen geometry in a silicone block, but used a mold to fabricate expendable alloy cores rather than 3D printing the core.

Extensive efforts were made to fabricate a compliant silicone model of a human aorta that represented the average geometrical and mechanical properties derived from literature (Marconi et al, 2018). Here the idea was to understand the impact of common pathologies and therefore the authors insisted on working with general mechanical and geometrical configurations. The authors considered the aorta from the root to the proximal part of the iliac arteries and do not include the vertebral arteries. The design was done using SolidWorks software and the molds were 3D printed, as applied by previous researchers. Sylgard 184 was used to fabricate a model with a high degree of match of the thicknesses between the construct and the CAD models. Thus, it is a success story of fabricating model of an average healthy aorta. However, the authors are yet to test their methodology in constructing patient-specific models and have proposed to explore its applicability in the future.

Peattie (2016) et al. constructed rigid, thick-wall and flexible, thin-wall phantoms replicating the patient AAA shape with the renal and iliac arteries. The rigid phantom was fabricated using the lost-core casting technique, while the flexible phantom was fabricated using a new method. a hollow 3D replica of the wall was printed in ABS plastic by fused deposition modeling with a 3D printer. This replica served as a positive vessel wall in further molding steps. The interior surfaces were then coated with a thin layer of spray-on mold release. It was then filled with sculpting wax. This represented a solid wax mold of aneurysmal aortic lumen with its renal and iliac branches. Then silicone rubber block was cast around the outside of the wax filled wall positive. Followed by this, the wax filled wall positive was removed from the silicone rubber block and the wax lumen was re-suspended inside the rubber block leaving a uniform gap. Injection molding was done in the silicone mold and the wax lumen was melted out after the silicone elastomer cured. The final flexible phantom was obtained. The authors carried out wall pressure measurements on both the phantoms and computed the wall internal stress. Sulaiman et al. (2008) and Chueh et al. (2008) also fabricated silicone phantoms using an injection molding technique.

2.3 Summary of Literature Survey

Different techniques and methods were employed to fabricate patient specific replicas of different vascular systems to carry out in-vitro studies for suitable interventions. The main manufacturing techniques are rotation coating, core-shell and lost-core casting. However, each technique has its own merits and demerits, such as non-uniform thickness (Karina et al. (2008), Hütter et al. (2016)), not having the desired wall thickness (Hütter et al. (2016)), rigid walls (Ruedinger et al. (2019), Watts et al. (2007)) and high cost (Karina et al. (2008), leaving scope for further research to construct accurate replicas.

2.4 Patient-Specific Model Reconstruction

The patient selected for the study was based on Type II endoleak indication and was imaged before and after the endovascular aneurysm repair procedure. All imaging was acquired by contrast-enhanced spiral CT (model Discovery CT750 HD Scanner, General Electric Healthcare, Inc., Waukesha, WI), with a nominal slice thickness of 0.625mm and a spiral pitch factor of 0.98. Three-dimensional models were developed by segmentation of the CT scans using the semiautomatic threshold-based segmentation tool of the open-source program ITK-SNAP (Version 3.6.0; www.itksnap.org)). This software allows one to use the CT scans to generate a surface mesh. Separate segmentation masks were constructed for the lumen and the thrombus, neglecting the arterial wall. The segmented model, shown in Fig. 2.1, extended from the diaphragm level to the iliacs, including the superior mesenteric artery (SMA), arc of Riolan, renal arteries, lumbar arteries (LA), inferior mesenteric artery (IMA) and the iliacs. The LA, IMA and arc of Riolan were considered as retrograde blood flows from these arteries contributed to type II endoleaks post-EVAR. The curvature of the lumbar arteries were neglected and replaced with ideal straight cylindrical vessels as shown in Fig. 2.2.

The initial 3D representation of the lumen and thrombus combined was post-processed using Meshmixer (Meshmixer [online]. 2017 [cit. 2017-11-18].https://www.meshmixer.com) to smooth while maintaining accuracy. Our collaborator, who is a vascular surgeon, verified the segmentation process for accuracy. Branch vessels such as the lumbars, renals, SMA and iliacs were then separated from the main body for 3D printing. Suitable connectors were built at the vessel interfaces using Meshmixer for attachment. Different materials such as Polylactic Acid (PLA), Acrylonitrile butadiene styrene (ABS) and VeroClear, a PolyJet photopolymer were explored for 3D printing the model. Out of these, VeroClear was selected for fabricating the vascular replica using Stratasys Object350 Connex3 due to its high surface finish and ability to be used directly without further processing as shown in Fig. 2.3.

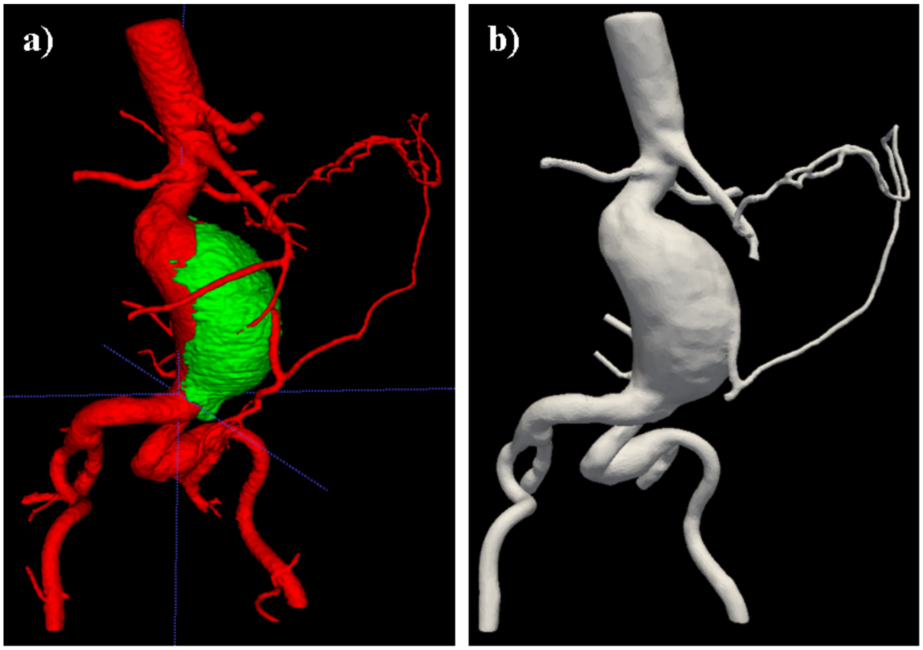

Figure 2.1: Patient geometry (a) Three-dimensional reconstruction of AAA segmented using ITK-SNAP including the lumen (red) and the intraluminal thrombus (green) (b) Final model smoothed using Meshmixer including superior mesenteric, renal, arc of riolan, inferior mesenteric, lumbar and iliac arteries.

Molds of the 3D printed parts were made using silicone rubber (Smooth-on Dragon Skin FX Pro, Smooth-on, Macungie, Pennsylvania, USA) as shown in Fig. 2.4. After curing, a suitably sized slit was made on the silicone rubber molds to remove the 3D printed replica. Fastform wax (Fastform casting wax, REMET Corporations) was selected for casting due to its high dimensional stability and excellent surface finish, which are desired properties to achieve an accurate, highly transparent silicone phantom. Wax pellets were heated in an oven to 82°C and parts were cast in the silicone rubber molds. Thick metal wire piece was used to reinforce the neck of the aneurysm model. Weight reduction of the wax model was done using aluminum foil pellets to reduce the volume of wax filling. This weight reduction reduces the eccentric load and aligns the center of mass with the axis

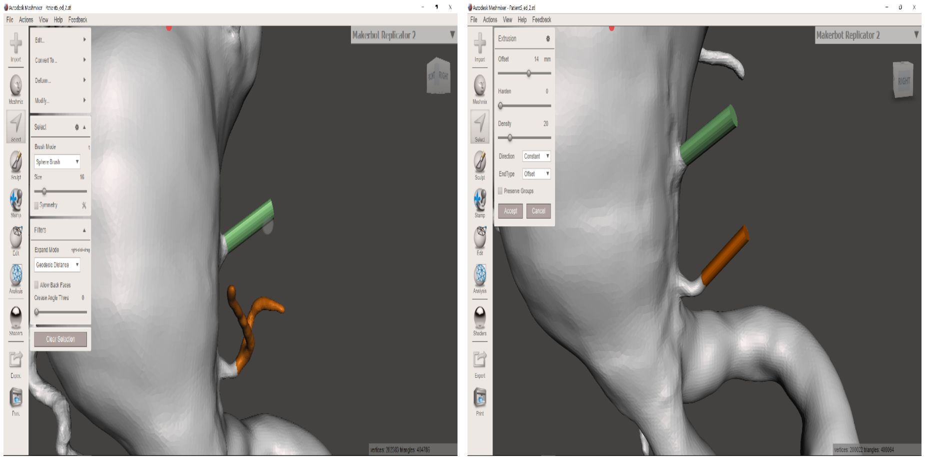

Figure 2.2: The two branches of the L3 and L4 lumbar arteries were replaced by an ideal lumbar cylinder geometry for manufacturing convenience.

Figure 2.3: 3D printed ABS parts of the entire model. The whole model was split into smaller parts with suitable connectors due to 3D printer restrictions.

of rotation of the model. The cast wax parts were smoothed using 75% ECOWASH PLUS solution (REMET Corporations), which is a solvent enchant ,and using a heat gun. During the smoothing process, care was taken to maintain dimensions of the original geometry.

The smoothed wax pieces were connected to form the entire model by locally melting the connectors incorporated using Meshmixer (as explained earlier) and connecting the various wax parts together. A final smoothing operation was carried out on the full wax replica using heat gun to remove the seams and give a smooth surface finish at the interfaces of the attached parts. The smoothed model tested for coating is as shown in Fig. 2.5.

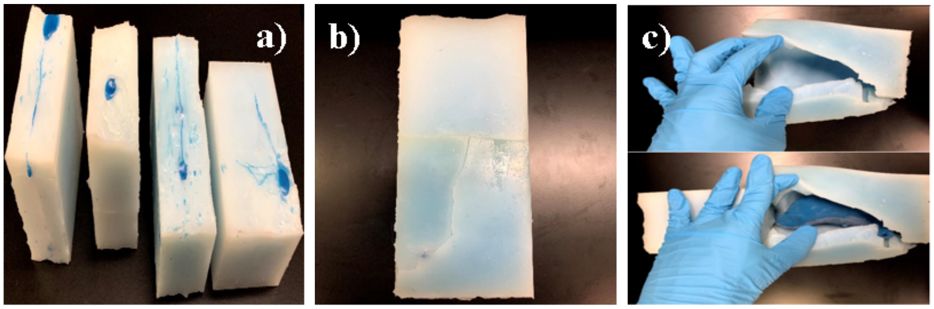

Figure 2.4: Silicone mold and wax model. (a) Female silicone mold formed using the 3D printed ABS model. (b) Mold filled with molten wax. (c) Solid wax model manufactured using the silicone mold.

Figure 2.5: Smoothed model

2.5 2-Axis Rotation Coating System

To manufacture the silicone model, a 2-axis rotation coating system was designed and assembled using SOLIDWORKS as shown in Fig. 2.6. The objective of the system is to provide a rotatory and oscillatory motion to produce uniform thickness of the silicone phantom.

It had the following parts:

a) Main shaft: It housed the stepper motor and is held between a servomotor on one end and a ball bearing at the other end. It was designed in SOLIDWORKS and 3D-printed in PLA. It changes cross-section from a 5 cm edged rectangle to a circle of 5 cm diameter, to fit within a ball bearing. It is designed with vents for heat dissipation from the stepper

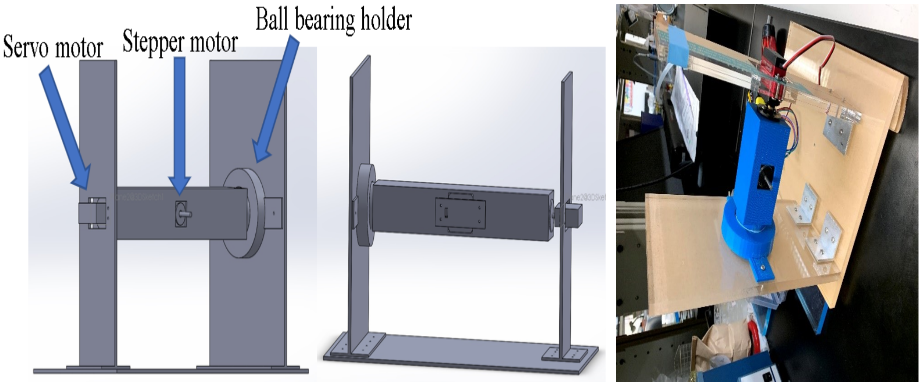

Figure 2.6: Two-axis rotation coating device used for manufacturing the silicone model.

motor.

b) Stepper motor: It is housed in the main shaft and has the wax replica attached to its spindle through a model holder. It is used to provide continuous rotation of the wax replica at a desired speed. Nema 17 Stepper motor is used and it provides a holding torque of 59 Ncm at 24V and 2 A. A Stepper motor is chosen over a DC motor as wobbly motion was observed using a DC motor. This is because the center of mass of the aneurysm does not lie on the axis of rotation and also due to the inability of of a DC motor to provide holding torque. The stepper motor is cooled continuously using ice packs and heat sink to allow continuous operation over 15 hours.

c) Servo motor: It is used to provide oscillating motion to the main shaft, which in turn oscillates the wax replica. It connects to the main shaft at one end through screws. ANNIMOS 20 kg digital servo motor is used and it provides a maximum torque of 21.5 kg-cm at 6.8 V and 2 A.

d) Ball bearing: It supports the oscillatory motion of the main shaft provided by the servomotor. It is held in place by a ball bearing holder which screws into the side wall.

e) Model holder: It is used to mount the wax replica on the stepper motor spindle. It is a hollow cylinder with circumferential holes for driving screws into the wax replica. The annular space between the model holder and the wax replica is filled with aluminum foil to eliminate wobbly motion. The model holder prevents the heat transmission from the stepper motor shaft to the wax model, thus protecting the wax model from damage.

f) Heating chamber: It is an insulating chamber within which the entire apparatus is placed. The chamber is heated uniformly using a LCD panel heater to maintain a temperature of 33- 36 °C to accelerate the curing rate of silicone.

The electronics used to control the system consists of the following parts:

a) Stepper motor driver: It is an actuator which can transform pulsed signal from the Arduino Uno controller into angular displacement signals used to control the stepper motor. TB6600 Stepper Motor Driver is used.

b) Arduino Uno: It is a microcontroller used to control the functioning of both the stepper motor and the servo motor. It enables users to provide inputs through push buttons and potentiometers and provides control signals to the stepper motor driver and servomotor to achieve the desired output. A separate Arduino Uno board was used for the stepper and servo motor.

c) Push buttons and Potentiometers: Push buttons were used to switch on and switch off the servomotor and stepper motor. This enabled to stop the servomotor at any angle while oscillating, which can be used to redistribute the silicone over the surface of the wax replica to prevent accumulation. Potentiometers were used to change the rotational speed of the stepper motor ,and the frequency of oscillation and amplitude of oscillation of the servomotor. A breadboard is used to link the buttons with Arduino Uno through wires.

d) LED screen: It is used to display the amplitude and frequency of the servo motor.

The circuit diagram is shown in Fig. 2.7. The rotation coating system setup during the model fabrication process is shown in Fig. 2.8.

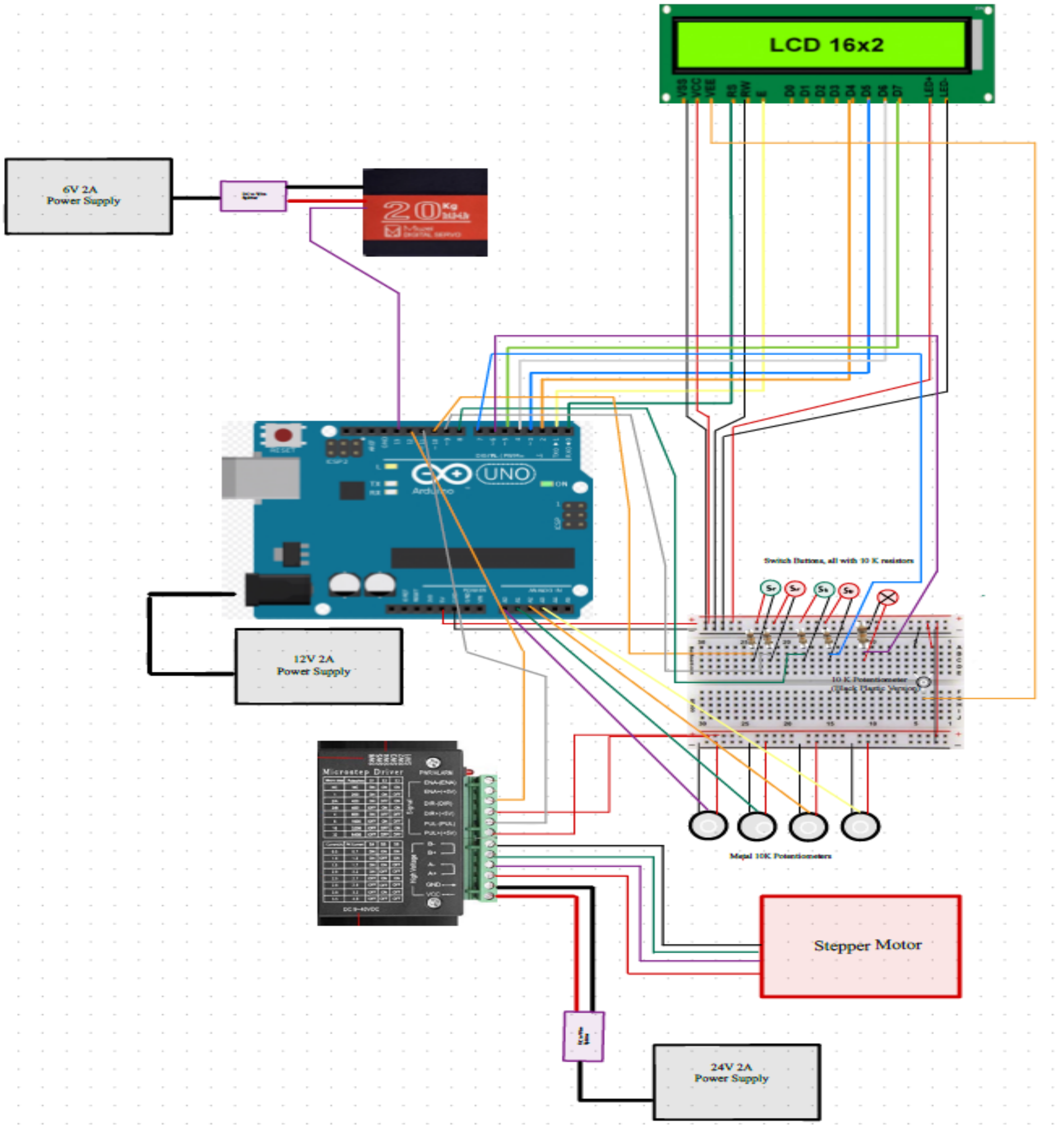

Figure 2.7: Circuit diagram of the 2-axis rotation coating system.

Figure 2.8: Two-axis rotation coating device during the silicone phantom manufacturing process

Table 2.1: Properties of Sylgard 184

Refractive Index	1.4118
Specific gravity	1.03
Modulus (MPa)	1.32-1.84
Ultimate tensile strength (MPa)	5.13-7.07

2.6 Phantom Fabrication Process

For the coating process, the small branch vessels such as SMA, IMA, renals, LA were neglected to standardize the model development procedure. Sylgard 184, a two-component silicone elastomer is used to fabricate the vascular phantom due to its low refractive index. Properties of Sylgard 184 is shown in Table 1. The fabrication process is summarized in the flowchart shown in Fig. 2.9. The coating procedure is detailed as follows:

1) The total quantity of silicone needed is first estimated based on surface area to be coated, thickness of the coating and the density of Sylgard-184. Through multiple trials, it was found that twice the volume calculated above was needed to account for spillage during

the process. It was desired to achieve a silicone phantom of 2mm thickness, which is the average thickness of the aorta wall (Humphrey et al. (2008)). The total silicone quantity was divided into a number of cups assuming a maximum of 18 g per cup and for each layer of coating, one cup of silicone was used. Using curing agent to elastomer ratio of 1:9, we can estimate the amount of elastomer and curing agent per cup. The coating process is organized based on surface area that 6 cups of silicone is used to coat the abdominal aorta and aneurysm body while the remaining 3 cups is used to coat the iliacs. In the total of nine layers, every third layer was coated on the iliacs.

2) The LCD panel heater is first turned on for one hour to uniformly heat the chamber as well as to warm the surface of the wax model.

Table 2.2: Parameters used for determining the silicone quantity required for rotation coating

Surface area to be coated	370 cm^2
Thickness of coating	0.2 cm
Volume of coating	74 cm^3
Density of Sylgard-184	1.03 g/cm^3
Estimated silicone quantity	76.22 g
Actual Silicone quantity needed	152.44 g
Total number of cups used	9
Amount per cup	16.93 g
Elastomer amount per cup	15.24 g
Curing agent amount per cup	1.69 g

3) Start with preparing 2 cups of silicone with the quantity 15.24 g of elastomer and 1.69 g of curing agent. Degas the two cups of silicone for 1 hour to remove all the air bubbles.

4) After degassing, the silicone was partially cured at 34°C before coating on the wax replica to reduce the rotation time of the wax model. Place 1 cup of silicone in the heating area for partial curing. Place the second cup inside the heating area after 1 hour of curing of the first layer. We number the cups for convenience. As a thumb-rule for subsequent layers,

we prepare each cup of silicone three hours before coating to allow 1 hour for degassing and two hours of partial curing before coating the layer of silicone.

5) After two hours of curing the first cup of silicone, the system is switched on and the speed of the stepper motor is set to 25 rpm. The speed of rotation of the stepper motor determines the uniformity of the silicone coating and depends on the strength of the wax model and the total time of coating. The optimal speed was found to be 25 rpm. While coating each layer, the servomotor is switched off and the wax replica is placed in the horizontal position.

6) The first cup of silicone is poured at a steady rate over the wax model from a height very close to its surface to prevent bubble entrapment. The silicone is poured only over the abdominal aorta and aneurysm body as the silicone gradually flows to the iliacs because of the geometry and servomotor oscillations. After pouring the first cup entirely, the servomotor is switched on. The servomotor amplitude is set such that sufficient gap exists between the surface of table and the lowest oscillatory position of the wax replica. Frequency of oscillation is set such that sufficient time is available for silicone to redistribute over the surface.

7) The coating is monitored every 10 minutes for any places of accumulation and the servomotor is stopped at appropriate angle of inclinations to allow the silicone to redistribute. Occasionally, speed of the stepper motor was also varied for a short duration to reduce accumulation.

8) 1 hour after coating the 1st layer, the wax replica is positioned horizontally using the servomotor and the 2nd layer is coated on the main body as described above.

9) The same procedure is repeated until the fifth layer. After the fifth layer, sufficient time (2 hours) is given for the silicone layers to cure into a jelly-like state before coating the next layer. This is done to prevent excessive spillage of the silicone.

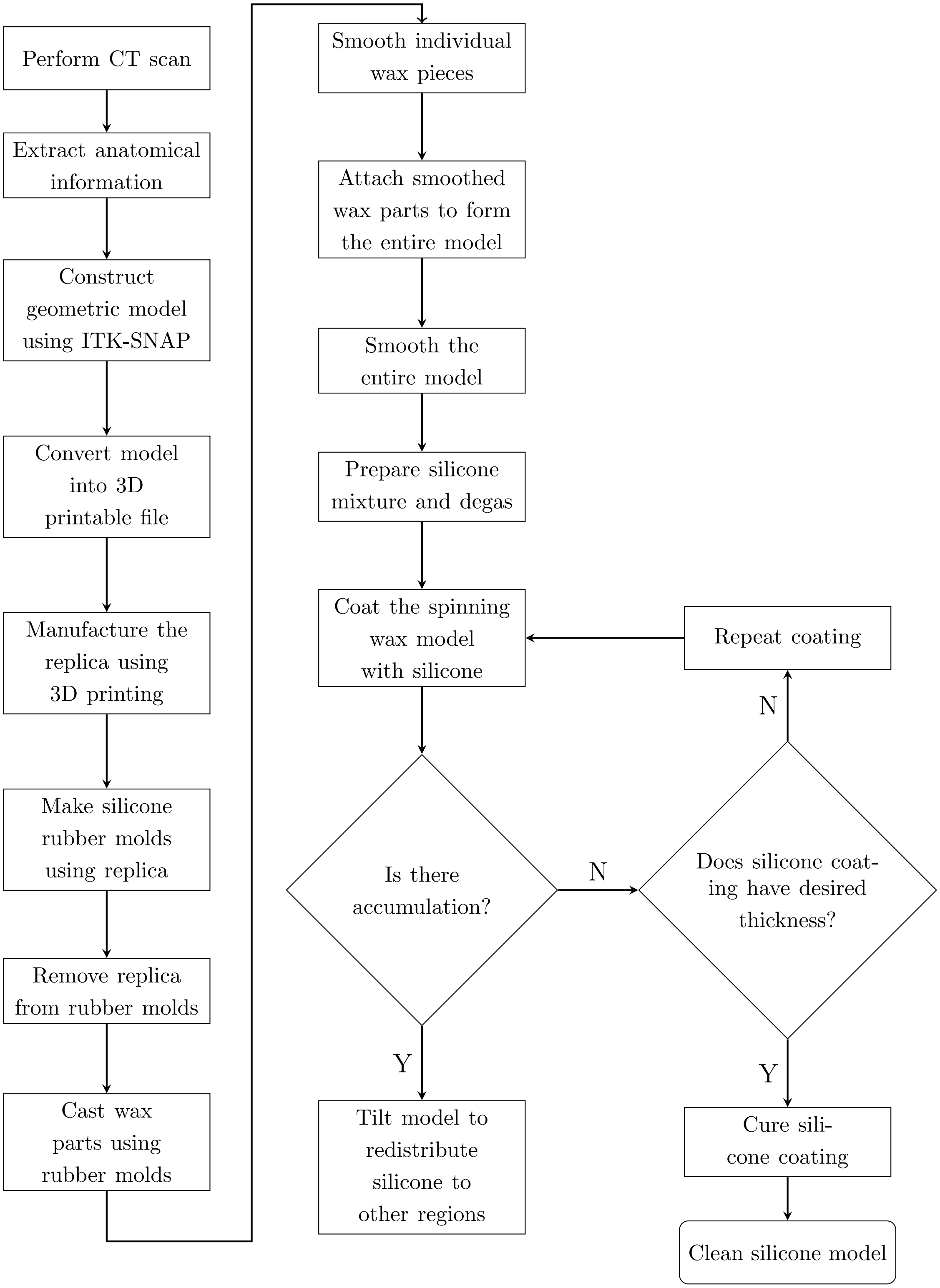

Figure 2.9: Model fabrication process flowchart

Figure 2.10: Silicone model (a) Silicone coated over the solid wax replica of the abdominal aortic aneurysm model (b) Wax melted out (c) Model after melting out wax (d) Cleaned silicone phantom

10) After two hours, the sixth layer is coated and hereafter a time interval of 1.5 hours was maintained between subsequent coatings.

11) After all the layers have been coated, the motor is switched off only after the silicone coating becomes jelly-like and reaches a state where it does not spill anymore.

12) The silicone coating is allowed to cure for 8 - 10 hours.

13) After curing for 10 hours, the silicone is still not completely cured. Now, a uniform coating is obtained over the abdominal aorta and aneurysm region, but still regions with less thickness are identified in the iliacs due to its complex geometry.

14) Sufficient amount of silicone is prepared in 1:9 ratio and added in regions of less thickness until sufficient thickness is achieved. This process is carried out while the entire system is switched off.

15) After achieving sufficient thickness, the silicone phantom is allowed to cure for 48 hours at 34°C. The cured silicone coated wax model is as shown in Fig. 2.10a.

2.7 Cleaning Process

The following procedure is used for getting a transparent model:

1) Melt wax completely out of the model by placing the silicone coated wax model within the oven at 82°C as shown in Fig. 2.10b.

2) Scrub walls of the silicone model against each other using 75% ECOWASH solution. Rinse the silicone model with water to remove the etched wax pieces.

3) Soak model in 75% ECOWASH solution for 24 hours to completely remove the wax adhered to the internal walls of the silicone model.

4) Rinse the model once in distilled water and soak the model in soapy water for 24 hours to remove the ECOWASH solution sticking to the model wall. There is also a possibility of the silicone turning yellow when the model is rinsed with hot distilled water. This yellowish tinge is removed when the silicone model is soaked in soapy water.

5) Rinse the silicone model thoroughly in distilled water to obtain a transparent silicone model as shown in Fig. 2.10d. Even though the silicone model develops a cloudy appearance when left exposed to air, it is completely transparent when submerged in water.

2.8 Discussion

A cost-effective manufacturing method of compliant silicone phantom has been developed. This method will be suitable when access to high quality 3D printers is not possible. It also reduces cost compared to dip-coating process proposed by Karina Arcaute et al. (2008) as it does not require the preparation of huge quantities of silicone needed for dip-rotation coating, most of which gets wasted. This method can be applied for patient-specific geometries as they are complex and various branch vessels lie on different planes which makes it difficult to use the core and shell technique for manufacturing silicone phantoms as it requires accurate positioning of the core within the shell to achieve a reasonably uniform thin-walled phantoms. Using our proposed method, a silicone phantom can be produced in around 10 days with the wax model development taking around 3 days, silicone coating procedure taking around 4 days and the cleaning process taking 3 days.

The thickness of the phantom was measured at multiple places and it was found to vary between 1.75 mm and 2.8 mm, with mean thickness of 1.9 mm thickness. Many other works (Karina et al. (2008), Hütter et al. (2016)) reported the same limitation of non-uniform thickness. A few air bubbles were observed in the aneurysm region, however, it is anticipated that this will not affect the PIV studies as stationary objects can be neglected during image processing. It was also difficult to control the silicone coating thickness of the silicone phantom below the iliac bifurcation as each of the branches revolve around the stepper motor axis and do not rotate about their own axis as the main body of the abdominal aorta, which makes it difficult to achieve a uniformly thick coating. The non-uniform thickness in the iliacs should not pose any problem as all the measurements are carried out in the aneurysm region and the purpose of including the iliacs is to reduce the effect of non-patient-specific boundary conditions and for the insertion of stent-graft.

This method will be successful for manufacturing vessel models with no bifurcation. This process can be made faster if the coating is carried out over a 3D printed anatomical model in materials such as Polyvinyl alcohol (PVA) as proposed by Ruedinger et al., which saves time involved in developing a wax replica. A DC motor can be used over stepper motor if the replica model is smaller in size or lighter in weight, eliminating heating issues for extended periods of operation. A custom model holder design can be developed for different models. With this method, a new high-quality casting wax was identified and a new protocol for cleaning the silicone model was developed. The 2-axis coating system is also inexpensive and the entire setup can be developed quickly.

For incorporating the model into the flow loop, connectors were incorporated at the ends of the iliacs as shown in Fig. 2.11. Suitable tube sizes that fit inside the aorta were

Figure 2.11: Full model with connectors attached at the outlets

identified for connecting to the inlet of the model in the flow loop circuit. The full model involving all the smaller vessels is to be coated in the future.

The thrombus inside the aneurysm can be replicated using a semi-porous silicone castable foam (Soma-Foama®, Smooth-on, Macungie, Pennsylvania, USA), which will be explored in the future.

2.9 Conclusions

A comprehensive literature survey on the patient specific phantom reconstruction indicated that a reasonable level of success is achieved, although there are variations in the constructed geometry. Thus, left a scope to further research for fabrication of a accurate patient specific phantoms to study the hemodynamics and further interventions required for clinical and surgical follow up.

In this work, reconstruction of patient specific silicone model of abdominal aortic aneurysm is experimentally demonstrated by adopting two-axis rotation coating method. A full model with connectors attached at the outlets have been fabricated successfully.

The chief advantage of the demonstrated methodology is that it avoids the wastage of the silicone elastomer (Sylgard 184), which is generally very expensive. The demerits of the method is the maintenance of non-uniform thickness across the phantom.

Bibliography

[1] Arcaute, K. & Wicker, R. B. Patient-specific compliant vessel manufacturing using dip-spin coating of rapid prototyped molds. *Journal of Manufacturing Science and Engineering, Transactions of the ASME* **130**, 0510081–05100813 (2008).

[2] Chivukula, V., Levitt, M., Clark, A., Barbour, M., Sansom, K., Johnson, L., Kelly, C., Geindreau, C., Rolland du Roscoat, S., Kim, L. & Aliseda, A. Reconstructing patient-specific cerebral aneurysm vasculature for in vitro investigations and treatment efficacy assessments. *Journal of Clinical Neuroscience* **61**, 153–159 (2019).

[3] Chueh, J. Y., Wakhloo, A. K. & Gounis, M. J. Neurovascular modeling: Small-batch manufacturing of silicone vascular replicas. *American Journal of Neuroradiology* **30**, 1159–1164 (2009).

[4] Humphrey, J. D. & Taylor, C. A. Intracranial and Abdominal Aortic Aneurysms: Similarities, Differences, and Need for a New Class of Computational Models. *Annual Review of Biomedical Engineering* **10**, 221–246 (2008).

[5] Hütter, L., Geoghegan, P., Docherty, P., Lazarjan, M., Clucas, D. & Jermy, M. Fabrication of a compliant phantom of the human aortic arch for use in Particle Image Velocimetry (PIV) experimentation. *Current Directions in Biomedical Engineering* **2**, 493-497 (2016).

[6] Marconi, S., Lanzarone, E., van Bogerijen, G., Conti, M., Secchi, F., Trimarchi, S. & Auricchio, F. A compliant aortic model for in vitro simulations: Design and manufacturing process. *Medical Engineering and Physics* **59**, 21–29 (2018).

[7] Peattie, R., Golden, E., Nomoto, R., Margossian, C., Pancheri, F., Edgar, E. & Dorfmann, A. A Technique for Comparing Wall Pressure Distributions in Steady Flow Through Rigid Versus Flexible Patient-based Abdominal Aortic Aneurysm Phantoms. *Experimental Techniques* **40**, 1187–1201 (2016).

[8] Ruedinger, K. L., Medero, R. & Roldán-Alzate, A. Fabrication of Low-Cost Patient-Specific Vascular Models for Particle Image Velocimetry. 10, 500–507 (2019). *Cardiovascular Engineering and Technology* **10**, 500–507 (2019).

[9] Sulaiman, A., Boussel, L., Taconnet, F., Serfaty, J., Alsaid, H., Attia, C., Huet, L. & Douek, P. In vitro non-rigid life-size model of aortic arch aneurysm for endovascular prosthesis assessment. *European Journal of Cardio-thoracic Surgery* **33**, 53–57 (2008).

[10] Watts, D., Sutcliffe, C., Morgan, R., Meagher, S., Wardlaw, J., Connell, M., Bastin, M., Marshall, I., Ramnarine, K., Hoskins, P. & Black, R. Anatomical flow phantoms of the nonplanar carotid bifurcation, Part I: Computer-aided design and fabrication. *Ultrasound in Medicine and Biology* **33**, 296–302 (2007).

[11] Yazdi, S. G., Geoghegan, P. H., Docherty, P. D., Jermy, M. & Khanafer, A. A Review of Arterial Phantom Fabrication Methods for Flow Measurement Using PIV Techniques. *Annals of Biomedical Engineering* **46**, 1697–1721 (2018).

Chapter 3

Setup of In-vitro Mock Circulatory Loop

3.1 Introduction

Mechanical factors and physiological changes in the aorta wall are known to cause rupture in AAAs. Therefore, it is necessary to investigate the flow induced wall stress distributions and the arteries leading to type II endoleaks through the study of flow patterns in physical models of aneurysms. In-vitro mock circulatory loop experiments are widely used to investigate the effects of the above mentioned mechanical factors. In in-vitro mock circulatory loop studies, it is possible to simulate the blood flow in diseased blood vessels, by means of a peristaltic pump replicating the pulsatility of blood flow, test fluid with similar properties of blood, a synchronized imaging apparatus to study flow patterns, and a model that accurately represents the anatomy of AAAs. This chapter describes the design and procedure that has been employed to set-up in-vitro mock circulatory loop in our laboratory.

3.2 Literature Survey

Liu et al (2005) designed a mock human circulatory loop to simulate various physiological conditions under healthy/rest, heathy/exercise. Healthy/sleep, Congestive Heart Failure (CHF)/rest, and partially recovered CHF/rest conditons. The objectives of their study are to predict the performance of prolonged Continuous Flow (CF) Left Ventricular Assist Devices (LVAD) under the beforementioned physiological conditions. The mock circulatory loop consisted of a pulsatile left and right cardiac simulators, windkessel chambers to simulate venous, arterial and pulmonary compliances, tygon tubes to replicate the venous and arterial segments, and finally a tuning clamp to mimic the total systemic peripheral resistance at different cardiac pressure/flow conditions. The hemodynamic parameters for different physiological cardiovascular conditions were measured, however the authors agree that due to the limitation of the variation in the volume of the diaphragm in the cardiac simulators, accurate prediction of LVAD performance was not possible.

The objectives of Gawenda et al's (2003) study was to assess the transmission of systemic pressure through the different types of graft material into the aneurysm sac. The authors set up an in-vitro circulation experiment consisting of an adjustable pulsatile pump, silicone tube, latex fusiform aneurysms, a cuff device, a windkessel and a collecting system. The study concluded that the aneurysm sac mean pressure increased with higher systemic pressure and its value depended on the type of graft material. This investigation highlighted the risk of aneurysm sac pressurization after endoluminal grafting and advocated further studies on endotension as well as non-invasive measurement of aneurysm sac pressure in the follow up of EVAR.

Once an aneurysm is developed, its expansion and rupture are due to an interplay between mechanical stimuli exerted by the pulsatile blood flow and physiological wall changes (Salsac et al 2006). Therefore, the objective of Salsac et al's study was to conduct an experimental investigation on the hemodynamic stresses acting on the vessel wall inside a healthy aorta as well as inside symmetric expanding AAA geometries made of glass. The experimental setup consisted of a programmable piston pump, a four-way pool valve to allow the pump to continuously empty one side of the cylinder and refill on the other side. A PIV-CAM was synchronized with the lasers and measures the location of the light scattering particles and from the digital images, the velocity field was calculated. The authors conclude that flow separation occurred right from early stages of AAA formation (D/d ¿1.3). The flow separation and strong vortex ring formation created perturbed stress distributed regions that do not occur in a healthy abdominal aorta. Two main regions of WSS patterns were identified- the detachment and reattachment region, whose size and location changes as the aneurysm grows.

Deplano et al (2007) attempted a similar study as Salsac et al (2006). The difference between their studies is that the former investigated the physiological flows with both rigid (glass) and compliant wall (polyurethane) asymmetrical AAA under resting and exercise flow conditions, while the later employed a rigid symmetrical AAA model. Deplano et al's experimental setup consisted of a computer-controlled pump, Millar catheters, electromagnetic flow meters, resistance element, compliance element, double pulsed mini Yag Laser, and a CCD camera. Glycerin solution containing 60 % water was pumped from an open tank to the AAA model immersed in a box of the same fluid. Interestingly, the authors concluded that unlike the rigid model, the compliant AAA model caused vortices to collide on the walls and contributed to increase in local pressure and wall stress. However, the serious limitation of this study as stated by the authors are that these models do not include iliac bifurcation and the thrombus insertion as the iliac bifurcation is known to cause increase in pressure and the intraluminal thrombus may contribute to reduced wall strength.

In a recent study, van de Velde et al (2019) reported the consequences of partial coverage on renal flow patterns and the wall shear stress. The authors used three models out of which one was control while the other two were stented, without and with partial renal artery coverage for comparative studies. Like earlier researchers, the authors conducted 2D PIV studies in a pulsatile flow loop to visualize flow in the renal artery under resting conditions. Here a sufficiently long tube was used before the model inlet for attaining fully developed flow profile and a two-element windkessel model was used to model distal vascular beds. The authors concluded that the stented models experienced low and oscillating wall shear stress, while the control did not, which may promote potential atherosclerosis and subsequent renal artery stenosis. The clinical significance of this study is the importance of avoiding renal artery coverage during the deployment of the main body.

Peattie et al (2004) attempted to understand the evolution of flow patterns and wall stresses by varying the AAA model bulge diameter similar to what has been observed clinically. The authors carried out the flow field and wall pressure measurements in seven fusiform AAA models of different bulge diameters under unsteady state conditions. The study concluded that the bulge diameter had significant influences on the AAA flow and wall stress. As the bulge diameter increased, unstable flow was experienced to a greater level with increased intensity. Vortices were formed in the bulge during the deceleration phase of systole, which then expanded in the retrograde flow phase. The study also noted maximum wall shear stress at peak systole at the distal bulge end.

Stamatopoulos et al (2011) investigated the unsteady flow of AAA by constructing a patient specific rigid transparent infrarenal aneurysm model with aorta-iliac bifurcation. The unsteady flow was created with a reciprocating piston. The hydraulic loop consisted of three liquid-air tanks, one upstream of the model and the other two on downstream of the model. 60 % glycerin-water mixture was the flowing medium, which was seeded with hollow glass spheres, which was illuminated by a 1 mm thick laser sheet. The authors measured the velocity field by 2D PIV which consisted of a pulsating laser, a camera and a synchronizer. The flow evolution in a cycle was then obtained by measuring phase average velocities in 14 planes. Aneurysm inlet, outlet and posterior wall experiences high shear stresses corresponding to the flow rate.

Deplano et al's (2014) work had an objective of mimicking the physiological flow rates and pressures by means of a shear thinning fluids in in- vitro experimental device through the bulge of complaint AAA model. Further, the aim is to characterize the rheology at low shear rates. The experimental work is designed in such a way that the selected fluid properties and the conformation of its molecular chains are preserved during the dynamics experiments. The setup had three interacting mock loops viz. circulatory loop, heating/cooling loop and the activation loop. In the circulating loop the working fluid flows from an open tank to flexible left atrium and ventricle models, an upstream compliant AAA model, and a downstream windkessel model and returned to the open tank. In order the mimic a mitral valve, a silicone 3-leaflet valve that divided the left atrium and ventricle are placed. The heating and cooling loop is to fix the temperature of the working fluid. The objective of the activation loop is to pump water from an open tank to the closed box containing the left ventricle box. The authors conclude that the flow dynamics was dependent on the flow rheology, thus a Newtonian fluid model is inadequate to predict the flow dynamics within the AAA.

3.3 Summary of Literature Study

- In vitro circulatory loop studies are the versatile experimental methodology used by many researchers for understanding the physiological cardiovascular conditions under healthy/rest, healthy/exercise, CHF/rest, and partially recovered CHF/rest conditions.

- Although the circulatory pulsatile mock loop studies helped to understand the flow dynamics, wall shear stress and pressure effects on different types of vascular diseases, intense research activities are seen even today due to the complexities of the diseases, and the desire to mimick in vivo conditions as closely as possible.

- The effect of stent geometries on the hemodynamics in rigid and compliant models were studied. However, studies with accurately constructed geometries of patient-specific phantoms are limited and the literature studies clearly opens further opportunities.
- In-vitro flow loop setup is an appropriate tool for identifying vessels leading to type II endoleaks post endovascular aneurysm repair of abdominal aortic aneurysms.

3.4 Design of Mock Circulatory Loop

A preliminary setup was constructed to create a aortoiliac bifurcation using 1" tygon tubes to understand the functioning of various components in the flow loop and maintain the desired pressure range. The components in the flow loop are:

2-element Windkessel: A two element windkessel consisting of a resistor and a capacitance element was used to mimic the systemic vascular resistance and the capacitance of the downstream vessels.

Resistor: A needle valve is used to control the mean pressure over the cardiac cycle.

Capacitance: An air-tight acrylic chamber with two ports- one connected to compressed air source to control the volume of air trapped within the chamber and another port connected to a pressure gauge to measure the air pressure. The height of the fluid in the chamber determines the pulse pressure and can be controlled by varying the volume of air trapped through the air port. The capacitance is designed based on the Liu et al. (2005)

and Kung et al. (2011) as follows:

$$C = \frac{dV_{fluid}}{dP_{fluid}} = \frac{V_{air}}{P_{air}} = \frac{V_{tank} - A_{tank}h_{fluid}}{P_{fluid} - \rho g h_{fluid}} \tag{3.1}$$

where C is the compliance of the tank

P_{fluid} is the absolute pressure of fluid in the tank

V_{air} is the volume of air in the tank

P_{air} is the absolute pressure of air in the tank

V_{tank} is the total volume of the tank

A_{tank} is the cross-sectional area of the tank

h_{fluid} is the height of the fluid in the tank

ρ is the density of the fluid

The chamber is designed based on the compliance value of a systemic arterial system for a healthy person, which is 2.2 mL/mm Hg and also based on a minimum value of 0.2 mL/mm Hg. There will be slight variation in the fluid level as the fluid enters and exits the compliance chamber, which results in an additional compliance in series with the compliance due to air compression. The varying fluid level results in a pressure change in the fluid given by

$$\Delta p = \rho g \Delta h = \rho g \Delta V/A \tag{3.2}$$

Thus, the compliance due to the varying fluid level is given by

$$C_v = \frac{A_{tank}}{\rho g} \tag{3.3}$$

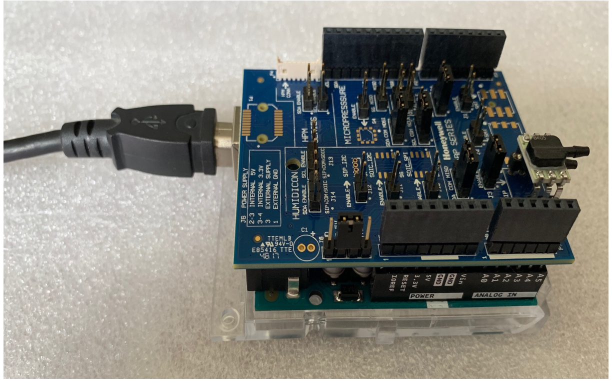

Figure 3.1: Pressure sensor setup

The A_{tank} is chosen such that C_v is huge compared to C_a, which is the capacitance due to air compression so that the total capacitance is approximately C_a as shown below

$$C_{total} = \left(\frac{1}{C_a} + \frac{1}{C_v}\right)^{-1} = \frac{C_a C_v}{C_a + C_v} \approx C_a \tag{3.4}$$

If we assumed the dimensions of the tank to be 13.5 cm X 13.5 cm X 13.5 cm and P_{fluid}= 100 mm Hg (860 mm Hg in absolute pressure), h_{fluid} should be 3.15 cm and V_{air}=1.886 L. So, if we maintain the height of the fluid to be 3.15 cm using the compressed air port, then we will achieve our desired compliance value. For compliance values of C=1.17, 0.9, 0.5 and 0.3 mL/mm Hg, h_{fluid} will be 8, 9.3, 11.2 and 12.1 cm respectively.

Pressure Sensor: A continuous monitoring pressure sensor was identified for pressure measurements inside the aneurysm. The selected pressure sensor is Honeywell ABP-DRRT005PG2A5 ($ 15.72/ unit). It is a high accuracy differential pressure sensor with a range of (0-5 PSI), +/- 0.25% accuracy, temperature compensated and has a response time of 0.46 milliseconds. A sensor evaluation kit, Honeywell SEK002 ($ 7.50/unit), has the code for directly evaluating the pressure sensor output. The pressure sensor is mounted on SEK002, which is plugged in as a shield board on Arduino Uno as shown in Fig. 3.1.

Open tank:A open tank with a capacity of 2.5 L was placed between the pulsatile pump

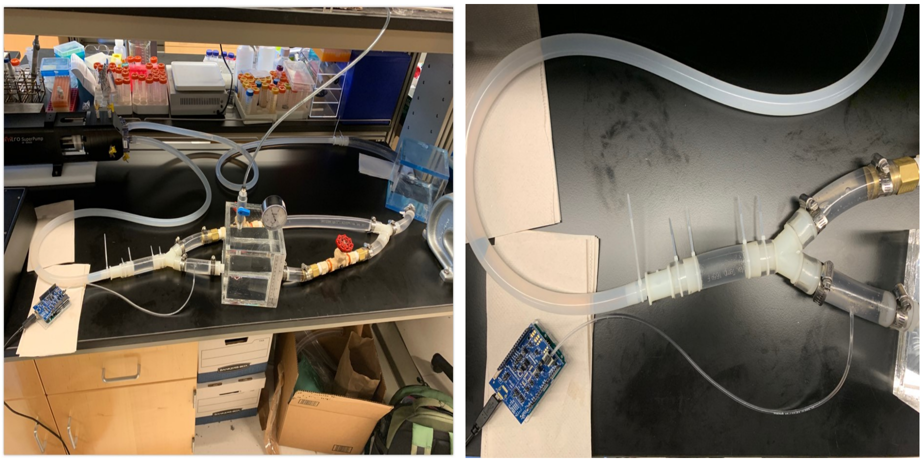

Figure 3.2: Setup for pressure test

and the resistor. The working fluid is supplied through the open tank. For the preliminary testing, tap water was used as the working fluid.

Peristaltic pump:A piston pump system (SuperPump System AR Series, ViVitro Labs, Inc., 455 Boleskine Road Victoria, BC, Canada V8Z 1E7) is used to precisely control the flow for this study. The pump has a range of stroke volume of 0-180 mL/stroke with 4% accuracy, and is capable of cycle rates of 3 to 200 beats per minute. The pump controller allows accurate control of the flow rate and frequency of the flow, and any desired flow waveform can be generated using the provided software (ViViGen software, ViVitro Labs, Inc.). The ViVitro Pump Head allows a uni-directional circulatory pulsatile flow loop. The ViVitro Pump head uses two spring-loaded disc valves and a silicone ventricle to isolate SuperPump piston fluid from the test fluid. The presence of the disc valves system on the pump system is very important part of the pump system since it allows for uni-directional flow similar to flows commonly observed in the circulatory system in human arteries.

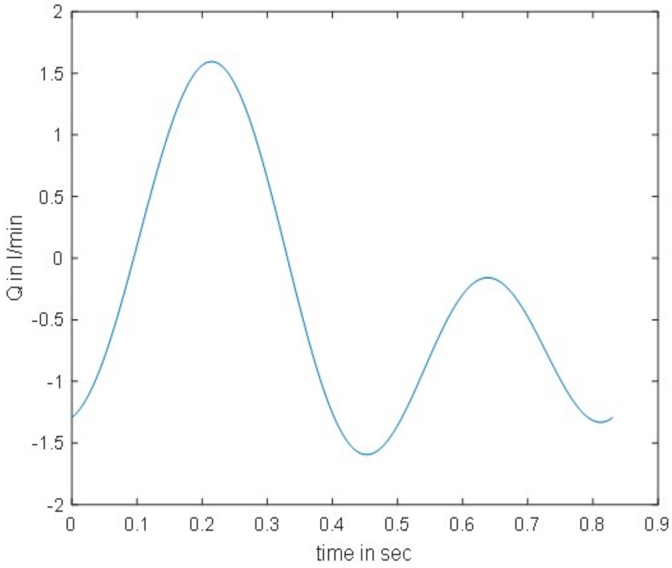

Figure 3.3: Flow rate profile input to ViVitro Superpump

3.5 Testing of Mock Circulatory Loop

The objective of the test was to maintain pressure in the range of 90 to 120 mm Hg in an aorto-iliac model setup as shown in Fig. 3.2. For the preliminary testing, the resting condition flow rate profile was adopted from Lee et al. (2003). For the input flow profile shown in Fig. 3.3, the capacitance and resistor elements were adjusted such that pressure varied between 90 to 120 mm Hg as shown in Fig. 3.4.

3.6 Discussion

A functional flow loop with two-element windkessel modelling of the distal vasculature has been constructed and accurate pressure measurements can be made. It has also been shown that with the proper tuning of the resistor and capacitance, pressure can be maintained in the desired range.

The flow loop for the final experiments was designed as shown in Fig. 3.5. All

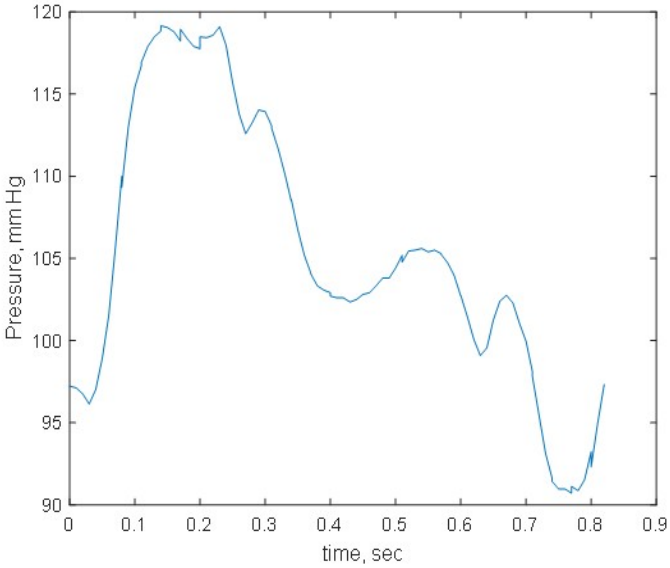

Figure 3.4: Pressure plot averaged over 20 cardiac cycles

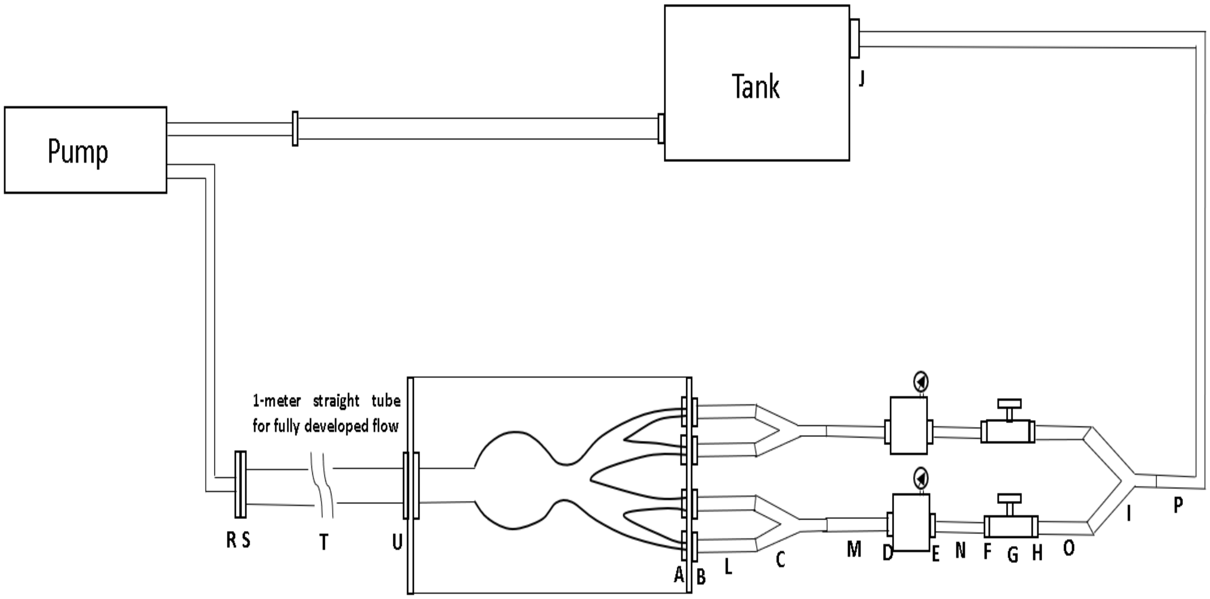

Figure 3.5: Designed flow loop

Table 3.1: Parts procured for construction of the flow loop

S.No.	Part	Required No.	McMaster Part/Marshalls Hardware	Package Quantity	Cost
A,B	3/8" x 3/8" Male barb	8	5372K118	10	5.07
C	Wye reducers 1/2"(A)x3/8"(B)	2	5463K732	5	12.86
D,E,J,R	$\frac{1}{2}$" x $\frac{1}{2}$" Male barb	6	5372K125	10	4.67
H,F	$\frac{1}{2}$" x $\frac{1}{4}$" male barbs	4	5463K465	10	5.09
G	$\frac{1}{4}$" Needle valve	1	Marshalls	1	9.29
I	$\frac{1}{2}$" Wye	1	Marshalls	1	4.39
L	Tube, 3/8" (ID)- $\frac{1}{2}$" (OD)	3 ft.	Marshalls	3 ft.	6.00
M,N,O,P	Tube, $\frac{1}{2}$" (ID)	5 ft.	Marshalls	5 ft.	13.80
S	1 Socket Female x 1/2 NPT Female	1	4880K083	1	1.65
T	1" (ID) Rigid tubing	3 ft.	49035K25	4 ft.	20.08
U	1 Socket Female x 1 NPT Male	1	4596K856	1	4.66
Total					87.56

components shown in Table 3.1 were procured and assembled. The flow loop consists of a 1" diameter straight rigid tube at the inlet for attaining a fully developed flow profile at the phantom entrance. The entrance length for fully developed womersley profile as found by Durst et al. (2005) is given by $[0.619^{1.6} + (0.0567Re)^{1.6}]^{1/1.6}$. Based on infrarenal location, the systolic Reynold's number is found to be 1944. Thus the entrance length is approximately 110 cm.

The entrance rigid tubing connects to the silicone phantom suspended within an acrylic box. The acrylic box is filled with the same fluid as the working fluid to prevent the refractive effects due to the model curvature. The working fluid selected matches the refractive index of the phantom's refractive index in addition to mimicking the properties of blood such as density and viscosity. Traditionally, aqueous glycerin solution containing 60% water (Deplano et al. 2007) and water-glycerin-NaI solutions are used as the blood mimicking fluid. The blood mimicking fluid considered in most aneurysmal flow studies used a Newtonian fluid approximation. Although, a recent study (Deplano et al. 2014) suggested that there was significant differences in the flow patterns and hemodynamic parameters between Newtonian and Non-Newtonian working fluids. The study suggested that the Newtonian fluid approximation cannot be made in aneurysmal flows because of the very low shear rates ($1sec^{-1}$) observed, at which the Non-Newtonian effects become significant.

Further, a recent study by Brindise et al. (2018) identified safer and economic Newtonian and Non-Newtonian fluid alternatives where the NaI salt is replaced by urea to avoid the high density solutions and discoloring effects produced by NaI. The study also suggested the use of xylitol as an alternative to glycerol as it is relatively safe and inexpensive. Hence, water-xylitol-urea solution in the ratios 50.9 Wt% water, 30.3 Wt% xylitol, 18.8 Wt% urea can be used as a Newtonian fluid with refractive index of 1.4118, viscosity of 4.033E-3 Pa.s and density of 1152 kg/m^3. For Non-Newtonian fluid, 0.02 Wt%

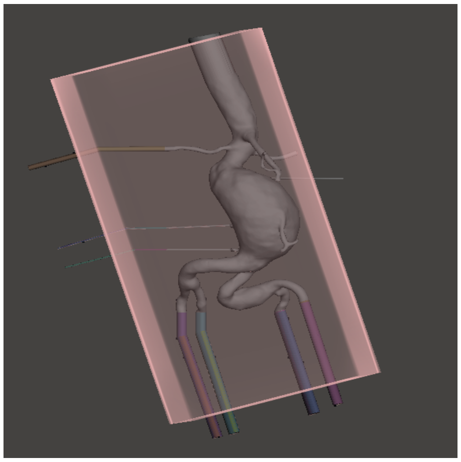

Figure 3.6: Model box design

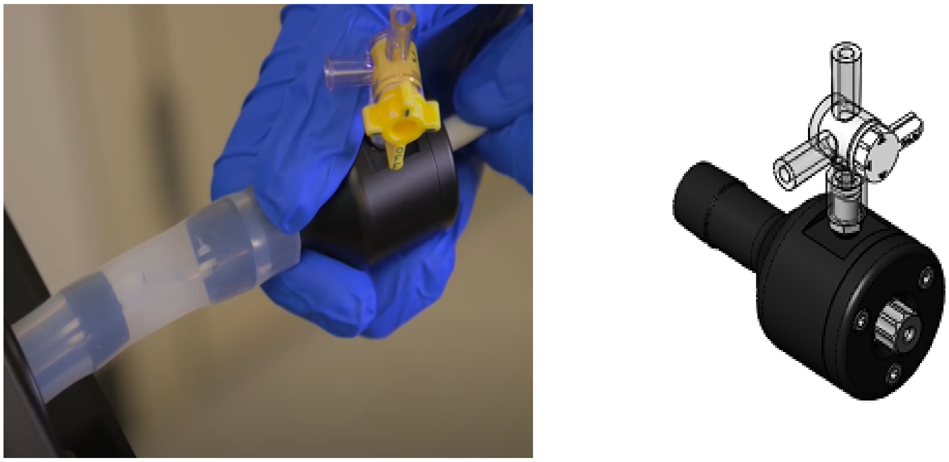

Figure 3.7: Catheter access port

Xanthan gum when added to water-glycerin-urea solution in the ratios 44.07 Wt% water, 34.52 Wt% glycerin and 21.41 Wt% urea can be used. Note that the Weight precentages holds true only when Xanthan gum is added at last to prepared water-glycerin-urea solution.

The box enclosing the aneurysm model was also designed as shown in Fig. 3.6. The particle image velocimetry system using suitable optics, laser and camera should be setup for measuring velocity in different planes in the aneurysm. For stent insertion procedure, the 26 French Catheter Access Port supplied by ViVitro Labs can be used as shown in Fig. 3.7. It has a barbed fitting inserting into a 1/2" ID tubing.

3.7 Conclusions

A comprehensive literature survey described the importance of in-vitro circulatory loop studies for understanding the physiological and mechanical cardiovascular conditions under healthy/res, healthy/exercise, healthy/sleep, CHF/rest and partially recovered CHF/rest conditions. Intense research activities continue even today due to the complexities of the diseases, and the desire to mimic the in-vitro conditions as closely as patient specific conditions. A functional flow loop with two-element windkessel modelling of the distal vasculature has been constructed and it can be employed for accurate pressure measurements. It has also been shown that with the proper tuning of the resistor and capacitance, pressure can be maintained in the desired range. Water-xylitol-urea solution in the ratios 50.9 Wt% water, 30.3 Wt% xylitol, 18.8 Wt% urea can be used as a Newtonian fluid. For Non-Newtonian fluid study, 0.02 Wt% Xanthan gum when added to water-glycerin-urea solution in the ratios 44.07 Wt% water, 34.52 Wt% glycerin and 21.41 Wt% urea can be used. Further a box to enclose the aneurysm model was also designed. Thus, an in-vitro mock circulatory loop is designed and set-up for feature flow- studies in our laboratory.

Bibliography

[1] Deplano, V., Knapp, Y., Bailly, L. & Bertrand, E. Flow of a blood analogue fluid in a compliant abdominal aortic aneurysm model: Experimental modelling. *Journal of Biomechanics* **47**, 1262–1269 (2014).

[2] Deplano, V., Knapp, Y., Bertrand, E. & Gaillard, E. Flow behaviour in an asymmetric compliant experimental model for abdominal aortic aneurysm. *Journal of Biomechanics* **40**, 2406–2413 (2007).

[3] Gawenda, M., Jaschke, G., Winter, S., Wassmer, G. & Brunkwall, J. Endotension as a result of pressure transmission through the graft following endovascular aneurysm repair - An in vitro study. *European Journal of Vascular and Endovascular Surgery* **26**, 501–505 (2003).

[4] Liu, Y., Allaire, P., Wood, H. & Olsen, D. Design and initial testing of a mock human circulatory loop for left ventricular assist device performance testing. *Artificial Organs* **29(4)**, 47, 341-345 (2005).

[5] Peattie, R. A., Riehle, T. J. & Bluth, E. I. Pulsatile flow in fusiform models of abdominal aortic aneurysms: Flow fields, velocity patterns and flow-induced wall stresses. *Journal of Biomechanical Engineering* **126**, 438–446 (2004).

[6] Brindise, M. C., Busse, M. M. & Vlachos, P. P. Density- and viscosity-matched Newtonian and non-Newtonian blood-analog solutions with PDMS refractive index. vol. 59 (2018). *Experiments in Fluids* **59**, 173 (2018).

[7] Salsac, A. V., Sparks, S. R., Chomaz, J. M. & Lasheras, J. C. Evolution of the wall shear stresses during the progressive enlargement of symmetric abdominal aortic aneurysms. *Journal of Fluid Mechanics* **560**, 19–51 (2006).

[8] Stamatopoulos, C., Mathioulakis, D. S., Papaharilaou, Y. & Katsamouris, A. Experimental unsteady flow study in a patient-specific abdominal aortic aneurysm model. *Experiments in Fluids* **50**, 1695–1709 (2011).

[9] van de Velde, L., Donselaar, E., Jebbink, E., Boersen, J., Lajoinie, G., de Vries, J., Zeebregts, C., Versluis, M. & Reijnen, M. Partial renal coverage in EVAR causes unfavorable renal flow patterns in an infrarenal aneurysm model. (2019).

Chapter 4

Image-based Computational Fluid Dynamics in Abdominal Aortic Aneurysms

4.1 Introduction

There are two types of modeling in Computational Fluid Dynamics (CFD): patient-specific CFD and image-based CFD. Patient-specific CFD refers to the use of patient-derived inflow and outflow boundary conditions in a patient-specific geometry for performing CFD. On the other hand, image-based CFD refers to the use of non-patient-specific inflow and outflow boundary conditions in a patient's geometry. Since, it is uncommon to obtain blood flow data during normal clinical practice, an image-based CFD was performed using inflow profile from literature. Through image-based computational fluid dynamics studies, the reason for thrombus initiation and deposition was explored through the study of shear quantities such as time-averaged wall shear stress, oscillatory shear index, endothelial cell activation potential and residence time.

4.2 Literature Review

The literature survey on Computational Fluid Dynamics (CFD) modelling to understand and accurately predict the intraluminal thrombus formation, the hemodynamics, wall shear stress, the rupture risk and the progression of the AAA from the its onset, has been vigorously pursued by four academic research groups within the USA, viz Prof Shadden (University of California, Berkley), Prof Alberto C Figueroa (University of Michigan), Prof J.D Humphrey (Yale University) and Prof. Amirhossein Arzani (Northern Arizona University).

CFD modelling was carried out by Di Achille et al (2014) to identify regions of formation of intra luminal thrombus (ILT) within AAAs with intact, yet susceptible endothelium. This study had the basis that two hemodynamic features had to coincide to promote the formation of a thrombus on an intact endothelium-platelets must experience a sufficiently high shear history and a susceptible endothelial region. The authors argue that the three separate metrics (TAWSS,OSI, PLAP) which are used to identify regions with low wall shear stress (WSS), oscillatory WSS, and high flow-induced particle shear history will be captured by the single newly proposed measure called the thrombus forming potential (TFP). Towards the utility of the new metric, the authors have shown computation results for carotid arteries, healthy infrarenal aorta and abdominal aortic aneurysm and found that that TFP accurately predicted regions susceptible to thrombus formation. The authors thus conclude that TFP will provide as a useful clinical metrics than simply a WSS-based parameter such as endothelial cell activation potential (ECAP).

The intraluminal thrombus (ILT) causes the aneurysmal wall susceptible to further dilation and rupture and hence Di Achille et al in the previous study introduced a new metrics called thrombus forming potential (TFP). Di Achille et al (2017) further elucidated the thrombus forming potential, its progression and the factors that affect the growth and remodeling of the aneurysmal wall through phenomenological metrics in this communication. The objectives of the authors work is to bring out the salient features of the competing effects of hemodynamically driven and hemodynamically-limited growth of ILT within the evolving AAAs so that appropriate clinical interventions could be designed. Di Achille et al for the first time introduced a new index called Thrombus Deposition Potential (TDP), for predicting the spatially-varying extend of deposition, as a phenomenological balance between the thrombogenicity of newly deposited thrombus and disruptive hemodynamic frictional forces. The combined results from thrombus forming (TFP) and deposition potential (TDP) in this study helped to locate the potentially thrombogenic regions. This study thus demonstrated the need to predict when and where thrombus might arise and the extent of its growth for a possible aneurysmal rupture-risk.

To avoid initiation and progression of AAA, lower extremity exercise is the best recommended therapy, which also favorably protects against atherosclerosis formation. Arzani et al (2014) investigated the topology of blood transport and compared it with mixing in five different patient specific AAAs during rest and exercise. The overall objective of this work is to uncover various features of unsteady chaotic flows that are not explored from traditional Eulerian characterization of blood flow. Lagrangian coherent structures were used here to investigate the mechanisms of advective transport. From the CFD modelling studies, the authors observed a prominent large scale flow featured in rest are removed in most cases during exercise. The important factor responsible for the changes in the flow topology of AAAs during exercise was the behaviour of the penetrating jet in systole. The jet either washed away recirculating regions or breakdown of the jet replaced recirculation regions with regions of chaotic mixing connected throughout the entire aneurysm. The authors also observed regions of closely spaced, (dense) LCS that caused enhanced mixing of the flow. These dense LCS could be associated with small-scale vortices due to mild turbulence. Thus, this study demonstrated direct quantification of mixing (particle resident time, PRT) based on the fresh blood that occupies the aneurysm and was found to be consistent to the results from the LCS. Higher mixing within AAA is beneficial while it is still not clear that poor mixing is adverse.

As discussed before, blood flow and hemodynamics influence the pathogenesis and pathophysiology of aneurysms. It is important to understand the flow stagnation and high residence time of biochemicals to characterize the complications like thrombosis and vessel wall inflammation in AAAs. It is a well-known hypothesis that low WSS and high RT are hemodynamic risk factors for vascular diseases. In a recent publication Arzani et al (2019) has brought the significance of different types of resident times (RT) such as particle residence time (PRT), Mean exposure time (MET), Eulerian RT (ERT), Virtual-ink RT (RT_{VT}), Eulerian indicator RT (EIRT) and Point-wise RT (RT_{PW}) obtained in CFD simulations using Lagrangian and Eulerian methods. The Lagrangian methods calculated flow stagnation via discrete particle tracking, while the Eulerian methods measure flow stagnation based on transport models and velocity measures. PRT showed least correlation with all of the other methods, since it was dependent on the characteristic length of the region of interest and does not rely on local flow stagnation. The RT_{PW} defines RT based on inverse of time-average velocity magnitude and gives a pure definition of stagnation. Out of all the above-mentioned methods, RT_{PW} and EIRT were the quickest methods to estimate RT and correlated well with each other. The authors conclude by reiterating that most of RT methods are conceptually different and should not be considered the same.

4.3 Summary of Literature Review

- Image-based computational fluid dynamics (CFD) modeling has become a popular method to study hemodynamics in lesions because of the high resolution and accurate estimation of near-wall parameters- a limitation of experimental measurements.

- Computational fluid dynamics (CFD) is used to delineate and predict aneurysm growth and rupture, thrombus formation and deposition potential based on hemodynamic metrics such as oscillatory shear index, wall shear stress, residence time etc.

- Two popular methods in aneurysm studies are Lagrangian and Eulerian Methods. Lagrangian studies are pursued to enrich the results from Eulerian methods.

- The role of intraluminal thrombus on aneurysm growth and rupture is unclear. Hence, it is important to understand how hemodynamics contributes to thrombus initiation and deposition.

4.4 Governing Equations

To perform CFD, the computational domain is discretized into tetrahedral elements and the blood is modeled as an incompressible fluid by Navier-Stokes equations as

$$\rho\frac{\partial v}{\partial t} + \rho v \cdot \nabla v = -\nabla p + \mu \nabla \cdot \nabla v \tag{4.1}$$

$$\nabla \cdot v = 0 \tag{4.2}$$

where the velocity v and pressure p are functions of space and time (x,t) and the density ρ and viscosity μ were assumed constant with values of 1.06 g/cm3 and 0.04 poise respectively. The blood is assumed to be a Newtonian fluid as Arzani et al. (2018) showed through the use of a novel Residence time- based non-Newtonian model for aneurysm simulations that shear-thinning effects were less in aneurysms and provided quantitatively and qualitatively similar results to Newtonian model. The study also concludes that the existing non-Newtonian models must be improved since they ignore rouleaux formation (aggregation of RBCs), a primary shear-thinning behaviour of blood.

4.5 Solver Methodology

All CFD simulations were performed using the open-source software, SimVascular (Updegrove et al., 2017). SimVascular solves the incompressible Navier-Stokes (N-S) equations using the Finite Element Method (FEM). The N-S equations are formed into a variational formulation and the Galerkin method is used for discretization. However, applying the Galerkin method directly onto the N-S equations results in unstable solutions due to the advective term, so additional stabilization is applied using the Streamwise Upwind Petrov-Galerkin (SUPG) method. The Newton's method is used to linearize the N-S equations to form a linear system of equations. This linearization naturally causes some errors. The residual error convergence threshold is thus the difference between the linearized solution found from Newton's method, and the full N-S equations with the non-linear advective term. Generalized-alpha method is used to advance the N-S equations in time, which is unconditionally stable and second order accurate for the N-S equations. The solver adds the squares of continuity and momentum residuals for each node and then calculates the root of mean squared residual.

4.6 Validation Cases

Two test cases were simulated in order to validate the solver as well as to finalize the various solver parameters.

4.6.1 Poiseuille Flow:

A steady simulation was conducted in a 4 cm diameter pipe whose length is 180 cm. The length of the pipe is slightly more than the entrance length. A plug flow profile with a flow rate of 100 cm^3/sec is prescribed at the inlet and a resistance boundary condition is prescribed at the outlet to obtain a pressure of 100 mm Hg. The Reynolds number is 884. The values of maximum velocity and wall shear stress from analytical equations are:

$$v_z^{max} = \frac{2Q}{\pi r^2} = 15.92 cm/s v_z^{avg} = \frac{v_z^{max}}{2} = 7.96 cm/s \tag{4.3}$$

$$\tau = \frac{2\mu v_z^{max}}{r} = 0.64 dynes/cm^2 \tag{4.4}$$

The simulation was conducted using a mesh consisting of 346991 tetrahedral elements for a mesh edge size of 0.48cm with 3 boundary layers. The time step was chosen such that the Courant–Friedrichs–Lewy (CFL) condition is satisfied as shown below.

$$CFL = \frac{v_{avg} * \triangle t}{\triangle x} = 0.166 < 1 \tag{4.5}$$

The number of non-linear iterations was chosen to be 5 and the residual criteria was set

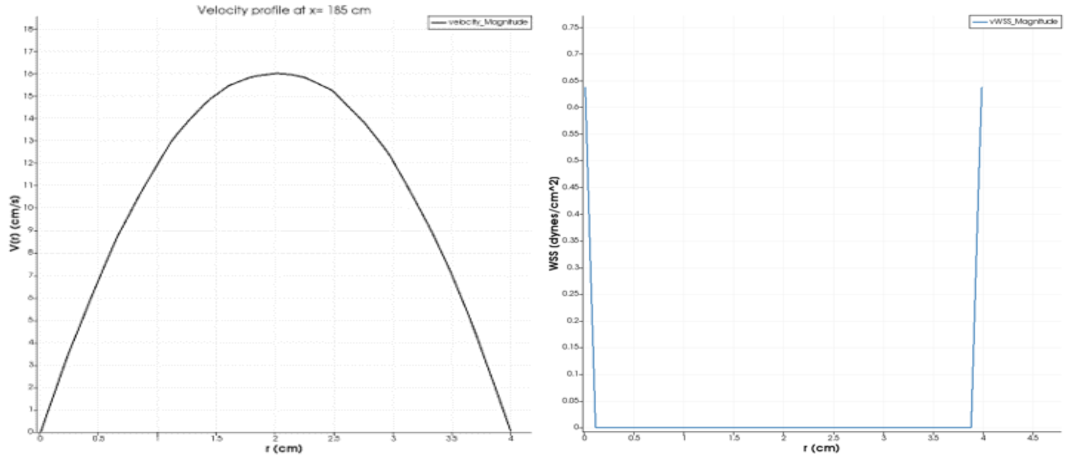

Figure 4.1: Velocity profile and wall shear stress profile at the pipe outlet (z=185 cm)

to be 10^{-4}. The simulation result was extracted at the outlet cross-section and gave a parabolic velocity profile with a maximum velocity of 16 cm/s. The wall shear stress was found to be 0.637 $dynes/cm^2$ as shown in Fig.4.1. Thus, the CFD results matched the analytical results.

4.6.2 Idealized Aneurysm Case:

The objective of this pulsatile simulation was to reproduce the time-averaged wall shear stress result reported by Gopalakrishnan et al. (2014) in an idealized aneurysm geometry, whose geometry is defined using the equation

$$r(x) = \left(\frac{D}{2} + Hexp\left(-\frac{x^2}{2W^2}\right)\right) \tag{4.6}$$

where the inlet section is 10D and the outlet section is 20D. The D is the diameter of the undialated sections, which is assumed to be 1.7 cm. H and W are the height and

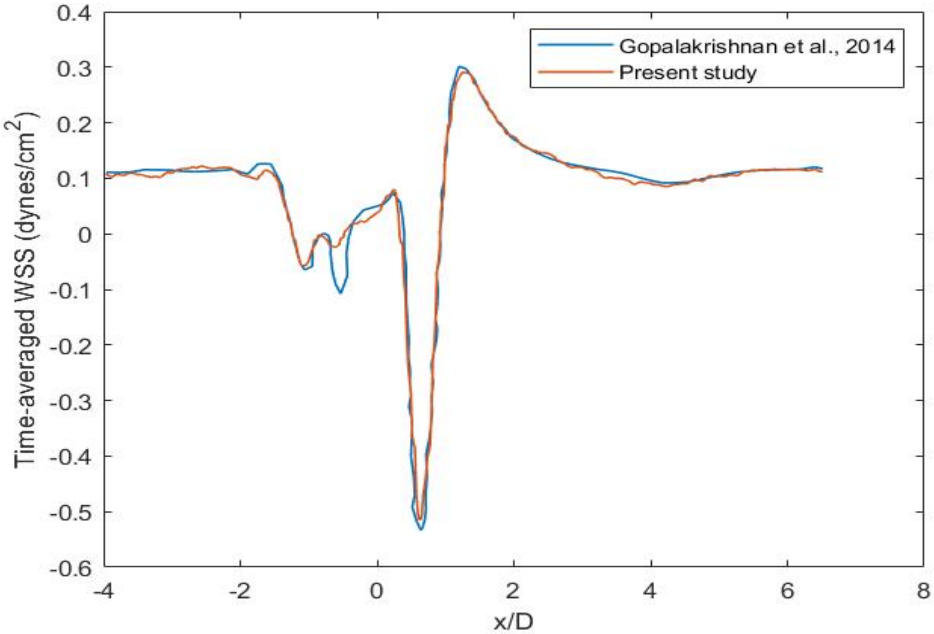

Figure 4.2: Time-averaged wall shear stress comparison

width of the aneurysm and they are both taken to be 0.5D. The pulsatile flow profile used by Gopalakrishnan et al. is assigned at the inlet and a resistance boundary condition is prescribed at the outlet. The mesh consists of 3.23 million tetrahedral elements with 5 boundary layers having a growth factor of 1.25 between subsequent layers. The simulation is run for four cardiac cycles to attain periodicity. The comparison of the time-averaged wall shear stress is shown in Fig. 4.2.

4.7 Numerical Methodology

The 3D patient-specific aneurysm surface mesh, used for the in-vitro experimentation, was modified for computational fluid dynamics simulatons. The aneurysm geometry started from the diaphragm level and included the celiac trunk (hepatic and splenic arteries), superior mesenteric artery, renal arteries, the arc of Riolan, lumbar arteries at L2,L3 and L4 levels, Inferior mesenteric artery and the iliac arteries (including internal and external arteries).The aneurysm geometry was considered from the diaphragm level as the aneurysm region introduced fluctuating flows and if the model begins at the infrarenal level, it would underestimate the transience in the flow inside the aneurysm. The vessel wall motion was assumed negligible since the abdominal aorta becomes stiffer with AAA progression due to an increase in collagen and decrease in elastin, and often an increase of intraluminal thrombus. A no-slip boundary condition is applied at the walls. Les et al. (2010) performed PC-MRI measurements at the supraceliac (SC) and infrarenal (IR) levels in 36 AAA patients and reported an average flow rate profile at SC and IR locations. The reported SC mean flow profile was mapped to a womersley velocity profile and was applied at the model inlet. The 24 data points reconstructed using PC-MRI over the cardiac cycle is shown in Table 4.1, and is interpolated to 201 data points to have a smooth representation of the inflow wave mapping to velocity vectors at the inlet face. 15 Fourier modes is used for curve fitting and the total cardiac cycle period is 1 second.

Table 4.1: Inflow condition at Supraceliac inlet

Time (s)	SC Flow (mL/s)	Time (s)	SC Flow (mL/s)
0	-11.8	0.5217	-9.19
0.0435	-13.1	0.5652	-15
0.0870	-19.5	0.6087	-18.6
0.1304	-96.1	0.6522	-18.9
0.1739	-204	0.6957	-18.4
0.2174	-203	0.7391	-18
0.2609	-172	0.7826	-15.3
0.3043	-136	0.8261	-14.7
0.3478	-103	0.8696	-13.7
0.3913	-60.9	0.9130	-14
0.4348	-20.2	0.9565	-13.7
0.4783	-4.75	1	-14.6

4.8 Outflow Boundary Conditions

The model consists of 16 outlets and three-element windkessel model was applied at each of the outlets. The three-element windkessel model consists of a proximal resistance (Rp), capacitance (C) and distal resistance (Rd), which were used to mimic the resistance and capacitance of the proximal vessels, and the resistance offered by the arterioles and capillaries, respectively.

The boundary conditions were prescribed according to Les et al. (2010). It is described as follows:

a) The patient's brachial diastolic blood pressure (DBP) and systolic blood pressure (SBP) was assumed to be 90 mm Hg and 140 mm Hg, respectively. The SBP and DBP at the model inlet was assumed to be same as the brachial DBP and SBP.

The mean pressure is found as shown

$$P_{mean} = \frac{SBP + 2 * DBP}{3} \tag{4.7}$$

Based on this mean pressure, the total resistance was found to be 2778.36 dynes.s/cm^2 using equation (4.8).

$$R_{totalsystem} = \frac{P_{mean}}{Q_{averageSC}} \tag{4.8}$$

b) The total capacitance was estimated using the pulse pressure method proposed by Stergiopolus et al. (1999). Briefly, the two-element windkessel equation (equation (4.9)) is solved for the pressure profile with flowrate profile given as input. The total capacitance is adjusted to fit the desired pressure range. However, since this equation does not take into account the geometry of the simulated domain, this method showed considerable deviation from the pressure range obtained from the CFD simulation. Hence, total capacitance was iteratively varied to get to the desired pressure range.

$$\frac{P(t)}{R_{totalsystem}} + C_{totalsystem}\frac{dP(t)}{dt} = Q(t) \tag{4.9}$$

c) The difference between mean supraceliac and mean infrarenal flow rate was distributed as 33.0% to the celiac trunk and 22.3% to the superior mesenteric artery and each of the renal arteries. Infrarenal flow was to be split between the 5 lumbar arteries, inferior mesenteric artery and the internal and external branches of the left and right iliac arteries.Based on Espahbodi et al. (2006), the mean systolic velocity through L2, L3 and L4 level lumbar arteries were assumed to have the same value of 16.9 cm/sec. Assuming that the flow rate profile for lumbar arteries varies similar to the inlet SC flow profile, the mean flow rate to each of the lumbar branches (with a diameter=0.25 cm) is found as.

$$Meanlumbarflow = \frac{Peaklumbarflow * MeanSCflow}{PeakSCflow} = 0.21ml/sec. \tag{4.10}$$

From Ku et al. (1994), the flow rate to the inferior mesenteric artery was found to be 2.167 mL/sec. After distributing the flow to the lumbar arteries and the inferior mesenteric artery, the rest of the infrarenal flow is distributed equally between the iliac arteries, and subsequently 70% of common iliac flow was distributed to the external iliac and 30% to the internal iliac arteries. The total resistance at each outlet (Rtot) was set to the patient's mean brachial pressure divided by the expected flow rate of the outlet. The resistance ratio Rp/Rtot was set to be 5.6% (28% for the renal arteries to avoid retrograde diastolic flow), which enabled the calculation of the proximal (Rp) and distal (Rd) resistances, where Rtot=Rp+Rd.

d) The total capacitance of the system is distributed to each outlet proportional to the target flow rate to each of the outlets.

The values of the RCR boundary conditions are shown in Table 4.2. CFD simulations were conducted in aneurysm wall (including the volumes of lumen and intraluminal thrombus) and lumen geometries to simulate flow before and after thrombus deposition. This can be used to explain mechanism of ILT deposition and the effect of ILT on wall shear stress.

4.9 Steady Simulations

The meshing of the computational domain is done using Tetgen meshing on SimVascular. A mesh with a global edge size of 0.2 cm was created and steady simulation was carried out with R_{tot} prescribed at the model outlets. The results of this simulation was used to generate an adapted mesh using the Adaptive meshing module on SimVascular. A new

Table 4.2: Values of boundary conditions. All units in CGS.

Outlet	R˙tot	R˙p	C	R˙d
Hepatic	26019.518	1457.093	7.327e-05	24562.425
Splenic	26028.090	1457.573	7.327e-05	24570.517
Superior Mesenteric Artery 1	35143.842	1968.055	4.956e-05	33175.787
Superior Mesenteric Artery 2	36668.323	2053.426	4.956e-05	34614.897
Left renal	18597.868	5207.403	9.913e-05	13390.465
Right renal	18689.114	5232.952	9.913e-05	13456.162
L2 lumbar	695574.142	38952.152	2.770e-06	656621.990
L3 left lumbar	683812.149	38293.480	2.770e-06	645518.669
L3 right lumbar	696823.846	39022.135	2.770e-06	657801.711
L4 left lumbar	695120.815	38926.766	2.770e-06	656194.049
L4 right lumbar	691627.462	38731.138	2.770e-06	652896.324
Inferior Mesenteric	66346.373	3715.397	2.858e-05	62630.976
Left internal iliac	68279.982	3823.679	2.831e-05	64456.303
Left external iliac	29207.657	1635.629	6.605e-05	27572.028
Right internal iliac	68318.251	3825.822	2.831e-05	64492.429
Right external iliac	29190.970	1634.694	6.605e-05	27556.275

mesh was manually developed with regional refinements to replicate the adapted mesh to have control over the local sizes as well as to generate meshes with different global edge sizes. The lumen geometry had a mesh size of 0.8 million elements and the aneurysm wall geometry had a mesh size of 1.13 million elements. At the model inlet, a mean flow rate of 51.185 mL/sec was prescribed and was mapped to a womersley velocity profile. Steady simulations were carried out on these meshes for 200 time steps to match the target flow splits by adjusting the R_{tot} values at each outlet. A time step size chosen was 1/1000th of the cardiac cycle period and it was found to satisfy the CFL condition. The CFL condition shown below is based on the smallest edge size (0.01 cm) used in the mesh.

$$CFL = \frac{v_{avg} * \triangle t}{\triangle x} = \frac{9.3554 * 0.001}{0.01} = 0.936 < 1 \tag{4.11}$$

Solver parameters used are as follows:

Step Construction: 4

Minimum Required Iterations: 2

Residual Criteria: 0.0001

For the R_{tot} values shown in Table 4.2, the deviation from target flow rates was less than 2% as shown in Table 4.3. Similarly, the boundary conditions were slightly adjusted for aneurysm wall geometry such that the deviation from the desired flow splits is less than 2%.

Table 4.3: Target flow rates and flow rates from simulation. All units in CGS.

Outlet	Target flow rate	Flow rates from CFD	% deviation
Hepatic	5.5555	5.5696	0.25
Splenic	5.5555	5.5694	0.25
Superior Mesenteric Artery 1	3.7581	3.6963	-1.64
Superior Mesenteric Artery 2	3.7581	3.7461	-0.32
Left renal	7.5162	7.5206	0.06
Right renal	7.5162	7.5257	0.13
L2 lumbar	0.21	0.2104	0.18
L3 left lumbar	0.21	0.2105	0.22
L3 right lumbar	0.21	0.2104	0.18
L4 left lumbar	0.21	0.2104	0.18
L4 right lumbar	0.21	0.2105	0.22
Inferior Mesenteric	2.1667	2.1723	0.26
Left internal iliac	2.1463	2.1497	0.16
Left external iliac	5.0081	5.0169	0.18
Right internal iliac	2.1463	2.1496	0.15
Right external iliac	5.0081	5.0171	0.18

4.10 Pulsatile Simulations

Pulsatile simulations were carried out in the 0.8 million elements lumen mesh and the time-varying flow profile was assigned at the model inlet. At the outlets, RCR boundary conditions were prescribed. A series of simulations were performed with total capacitance of 0.5 mL/mmHg (as predicted by the Pulse Pressure method), 0.64 mL/mmHg, 0.8 mL/mmHg, 0.9 mL/mmHg, which was distributed to each outlet proportional to target flow rates. The simulations were run for 5 cardiac cycle to achieve periodicity in pressure waves and the simulation parameters used is shown in Table 4.4. The simulation results were stored for 50 time points in a single cardiac cycle. The pressure ranges at the model inlet for each of the total capacitance is shown in Table. 4.5. Out of the several trials conducted, a total capacitance of 0.9 mL/mmHg was chosen as the final value as it was closer to our desired pressure range of 90 and 140 mm Hg and also because the pressure usually changes 20-30% in an adult during a day. The pressure range was also representative of pressure in a hypertensive patient, which is a common health condition in people with aneurysms. The peak Reynolds number and womersley number based on the infrarenal location is found as follows:

$$Re_{peak} = \frac{4\rho Q_{peak}}{\pi \mu D} \tag{4.12}$$

$$\alpha = \frac{D}{2}\sqrt{\frac{\omega\rho}{\mu}} \tag{4.13}$$

where D is the mean diameter at the infrarenal section, Q_{peak} is the peak systolic flow rate at the infrarenal section, μ is the dynamic viscosity , ρ is the density, and ω is the angular frequency. The Re_{peak} and α was found to be 1944 and 12.8 respectively.

4.11 Hemodynamic Parameters of Interest

The time-averaged wall shear stress (TAWSS) is defined as

$$TAWSS = \frac{1}{T}\int_0^T ||\tau|| dt \tag{4.14}$$

Table 4.4: Solver parameters for pulsatile simulation

Parameters	Values
Step Construction	7
Residual Criteria	0.0001
Minimum Required Iterations	3
Tolerance on Momentum Equations	0.001
Tolerance on Continuity Equations	0.001
Tolerance on svLS NS Solver	0.001
Maximum Number of Iterations for svLS NS Solver	10
Maximum Number of Iterations for svLS Momentum Loop	20
Maximum Number of Iterations for svLS Continuity Loop	400

Table 4.5: Inlet pressure for different values of total compliance

Total Capacitance (mL/mm Hg)	DBP/SBP at inlet (mm hg)
0.5	80/162
0.64	85/160
0.8	87/157
0.9	90/153

where τ is the wall shear stress vector. Regions of low wall shear stress is susceptible to thrombus deposition.

The Oscillatory Shear Index (OSI) is used to describe the nature of shear stress. It is mathematically defined as

$$OSI = \frac{1}{2}\left(1 - \frac{||(1/T)\int_0^T \tau dt||}{\frac{1}{T}\int_0^T ||\tau|| dt}\right) \tag{4.15}$$

OSI value of 0 corresponds to a unidirectional shear stress and a value of 0.5 corresponds to a purely oscillatory shear stress. Regions with high OSI is susceptible to atherosclerosis and hence, can promote AAA growth.

Endothelial Cell Activation Potential (ECAP) proposed by Di Achille et al (2014) is used to capture regions that experience low TAWSS and high OSI. It is defined as

$$ECAP = \frac{OSI}{TAWSS} \tag{4.16}$$

Out of the various residence time measures discussed by Arzani et al. (2019), Point-wise Residence Time (RT_{PW}) proposed by Esmaily-Moghadam et al. (2013) was chosen to estimate residence time through an Eulerian approach. It is the inverse of time-average velocity magnitude at each point in the computational domain. If the velocity at a location is predominantly low, then residence time is high which in turn implies high flow stagnation at that location. Mathematically, it is represented as

$$RT_{PW} = \left(\frac{1}{T} \int_0^T ||v(x,t)||dt \right)^{-1} \tag{4.17}$$

4.12 Results

4.12.1 Pressures and Flows

All simulated flows were within 5 % of their target values and the SBP and DBP achieved at the inlet (as shown in Fig. 4.4.a) were within 10% of their target values. This is acceptable since pressure varies in an adult between 20 - 30 % on a normal day. The inflow profile validation is shown in Fig. 4.3.a and shows good agreement. Fig. 4.3. b-f and Fig. 4.4. b-f shows the outlet flows and pressures over the cardiac cycle from lumen geometry simulation. Since, similar outlet pressures and flows were observed in the aneurysm wall geometry, it has not been shown here. Further, anterograde flow was observed in the renal arteries as shown in Fig. 4.3.c and is in accordance with observations by Bax et al. (2005).

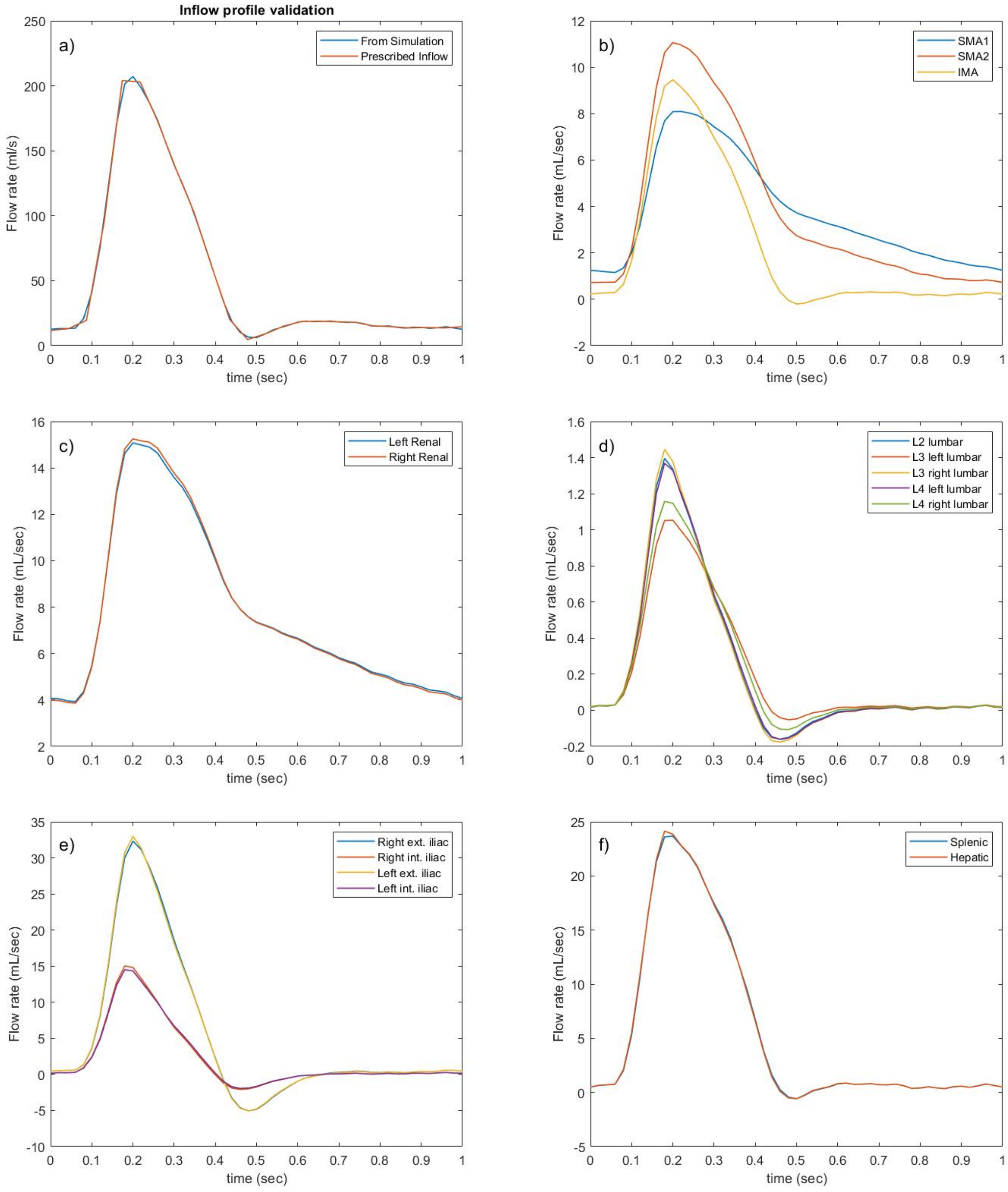

Figure 4.3: Inlet and outlet flow profiles over the cardiac cycle from lumen geometry simulation. a) Inflow profile validation b) Superior and Inferior Mesenteric flows c) Renal flows d) Lumbar flows e) Iliac flows f) Hepatic and Splenic flows

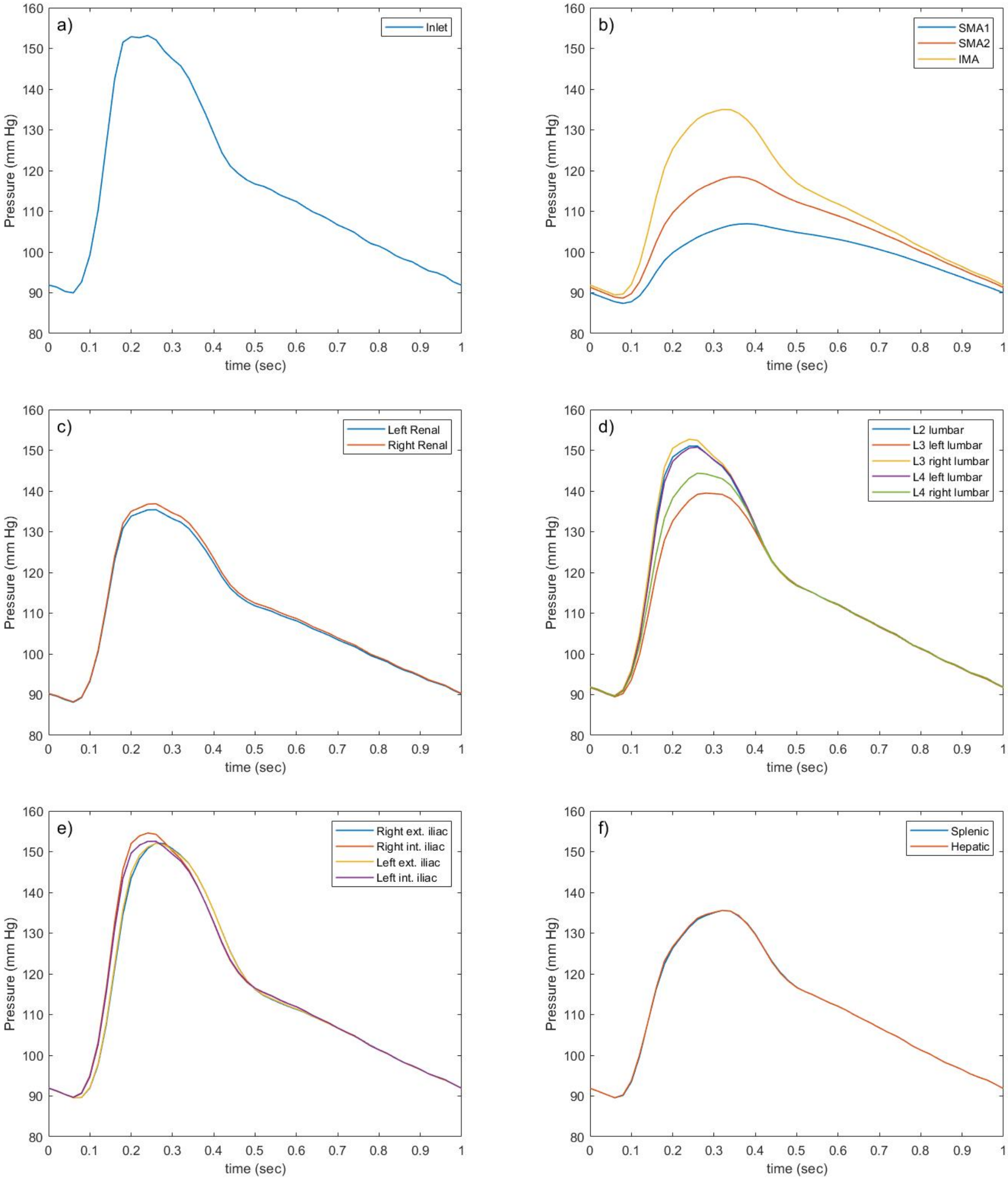

Figure 4.4: Inlet and outlet pressure profiles over the cardiac cycle from lumen geometry simulation. a) Inlet pressure. b) Superior and Inferior Mesenteric pressures c) Renal pressures d) Lumbar pressures e) Iliac pressures f) Hepatic and Splenic pressures

4.12.2 Flow Patterns

3D streamlines are shown in Fig. 4.5. and Fig. 4.6. to give a brief idea about the flow patterns in the aneurysm wall and lumen geometries at various time points (accelerating phase, peak systole and decelerating phase) in the cardiac cycle, respectively. It can be observed that the streamlines are organized at peak systole in both geometries. During the accelerating phase, streamlines are organized in the lumen geometry, whereas in the aneurysm wall geometry, mild swirling flow is observed. During the decelerating phase, flow separation from the anterior neck was observed and the streamlines follow the concave surface of the posterior wall. Velocity is always low in aneurysm region in aneurysm wall geometry due to the aneurysm expansion, which leads to low wall shear stress. This might lead to high Residence Time within the aneurysm.

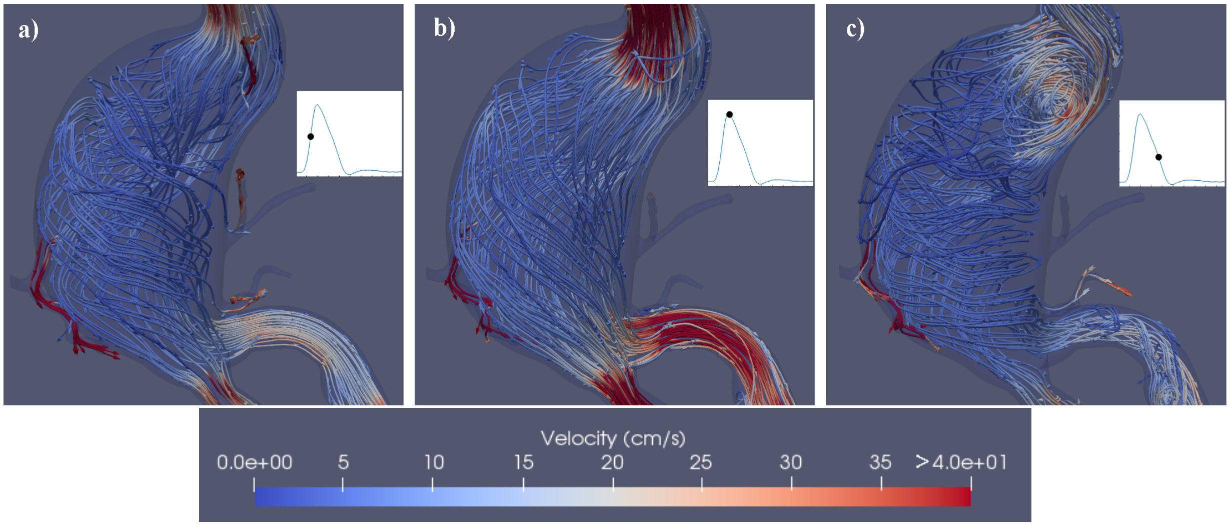

Figure 4.5: Streamlines at various times of the cardiac cycle in the aneurysm wall geometry. The streamlines are colored by velocity. a) Accelerating phase b) Peak Systole c) Decelerating phase

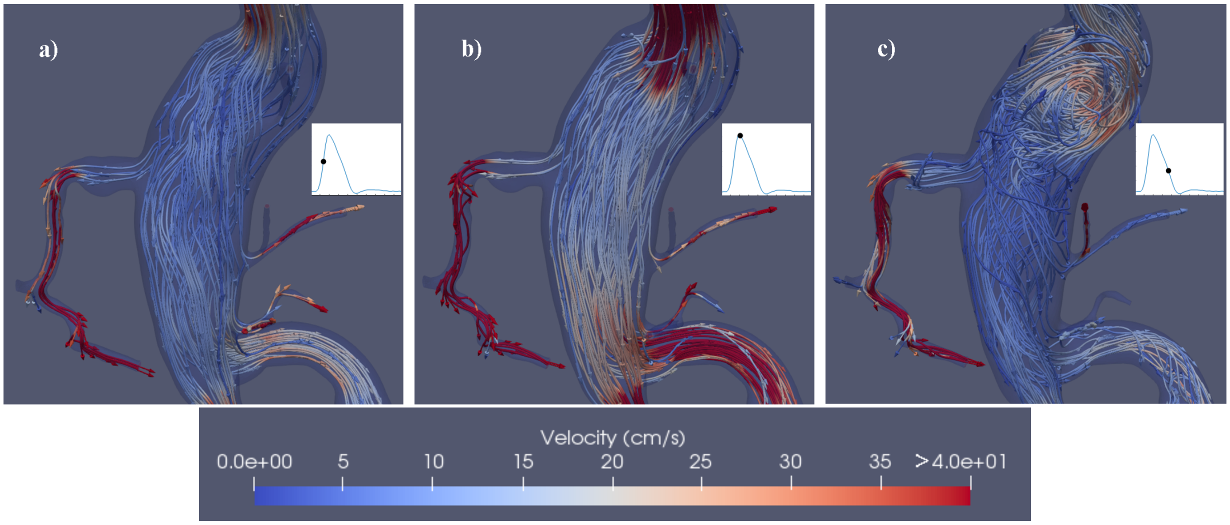

Figure 4.6: Streamlines at various times of the cardiac cycle in the lumen geometry. The streamlines are colored by velocity. a) Accelerating phase b) Peak Systole c) Decelerating phase

4.12.3 Time-Averaged Wall Shear Stress

The Time-Averaged Wall Shear Stress (TAWSS) is quantified in both the aneurysm wall and lumen geometries as shown in Fig. 4.7 and Fig. 4.8. In both Fig.4.7.b and Fig.4.8.b, peak values of wall shear stress is observed in the posterior wall of the aneurysm entrance. This is probably due to the jet impingement on the posterior wall of the aneurysm entrance. Also, as seen in Fig.4.7.d, low values of TAWSS is observed in the anterior wall of the aneurysm because of the reduced velocities due to the aneurysm expansion.

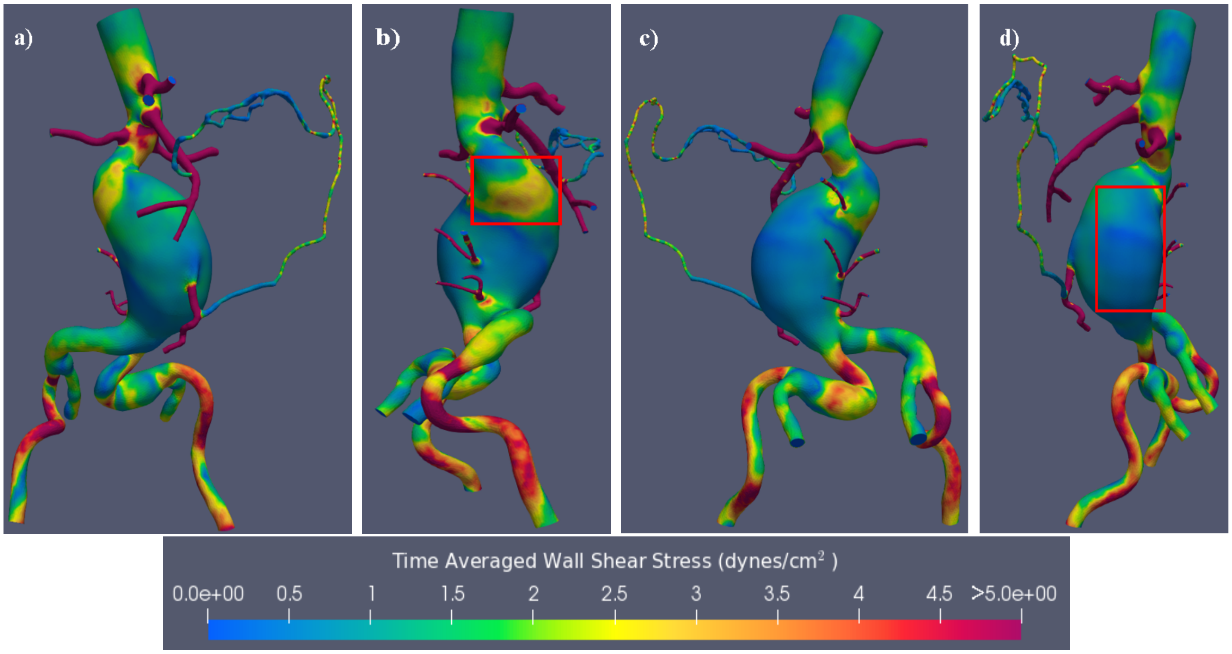

Figure 4.7: Time-averaged wall shear stress in the aneurysm wall geometry. a) Anterior view. b) Left lateral view. c) Posterior view. d) Right lateral view.

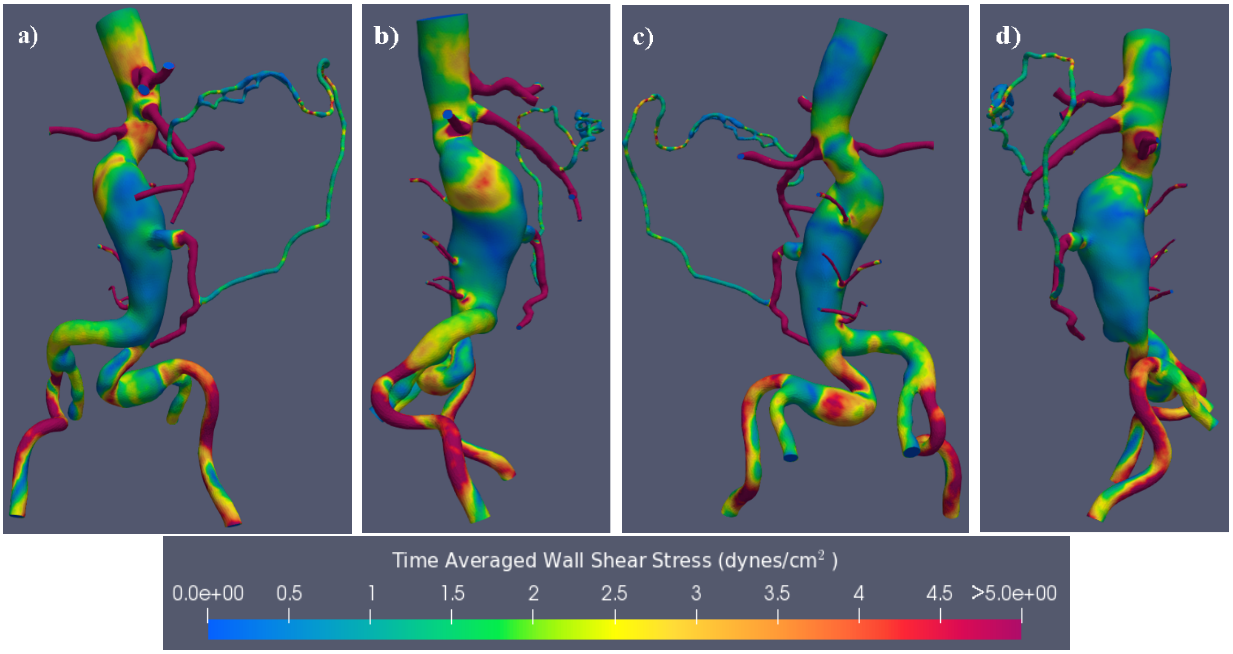

Figure 4.8: Time-averaged wall shear stress in the lumen geometry. a) Anterior view. b) Left lateral view. c) Posterior view. d) Right lateral view.

4.12.4 Oscillatory Shear Index

The unidirectionality of the wall shear stress is quantified through the Oscillatory Shear Index (OSI). Figure.4.9 and Figure.4.10 shows the Oscillatory Shear Index in both the aneurysm wall and lumen geometries, respectively. As highlighted in Fig.4.9.b and Fig.4.9.d, peak values of OSI is observed in the posterior neck, in the concave posterior surface as well as in the anterior wall of the aneurysm. It can also be observed that the OSI values are higher in the anterior wall of the lumen geometry compared to the anterior wall of the aneurysm wall geometry.

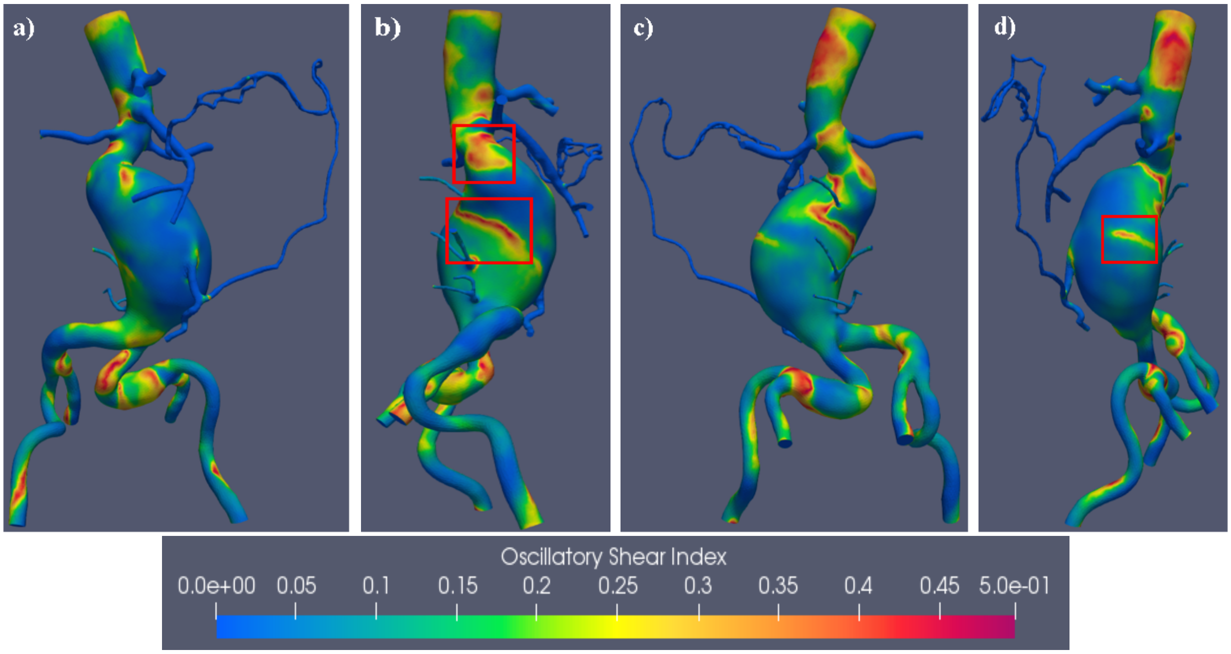

Figure 4.9: Oscillatory Shear Index in the aneurysm wall geometry. a) Anterior view. b) Left lateral view. c) Posterior view. d) Right lateral view.

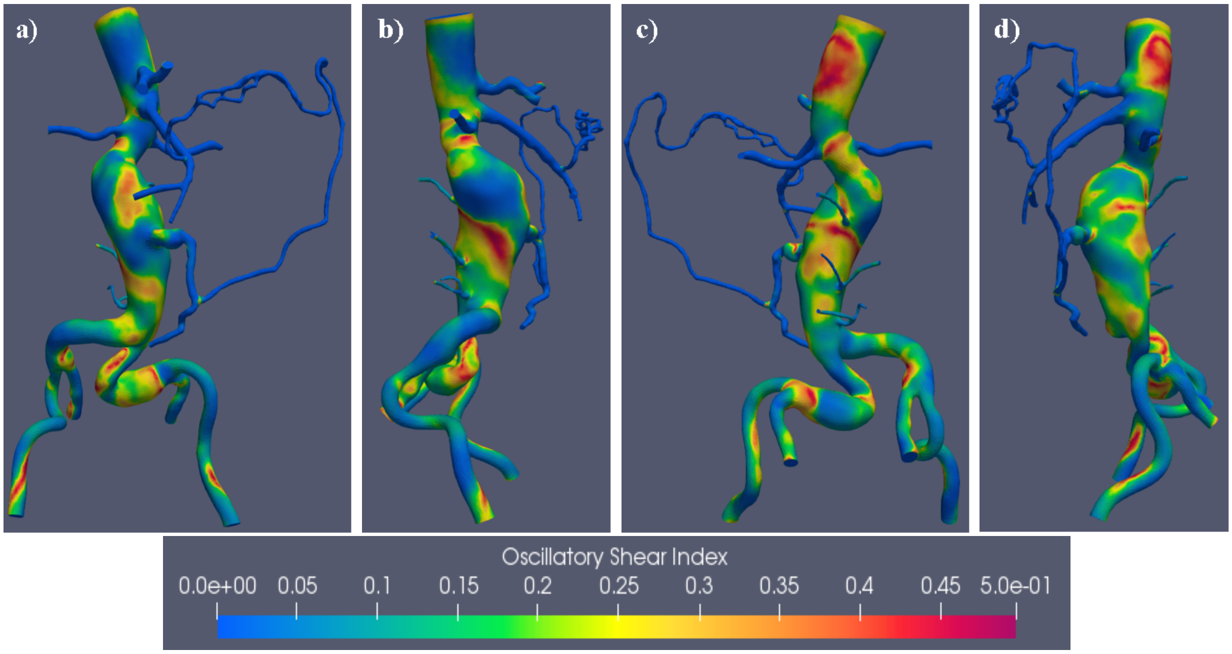

Figure 4.10: Oscillatory Shear Index in the lumen geometry. a) Anterior view. b) Left lateral view. c) Posterior view. d) Right lateral view.

4.12.5 Endothelial Cell Activation Potential

To find the regions of endothelial susceptibility, the Endothelial Cell Activation Potential is quantified in only the aneurysm wall geometry as shown in Fig. 4.11. ECAP is not quantified in the lumen geometry as endothelial cells generally line the aorta wall and there are no endothelial cells on the intraluminal thrombus surface exposed to the lumen. As observed in Fig. 4.11.b and 4.11.d, high values of ECAP can be observed in the anterior and posterior wall. These are places corresponding to regions of high OSI and low TAWSS.

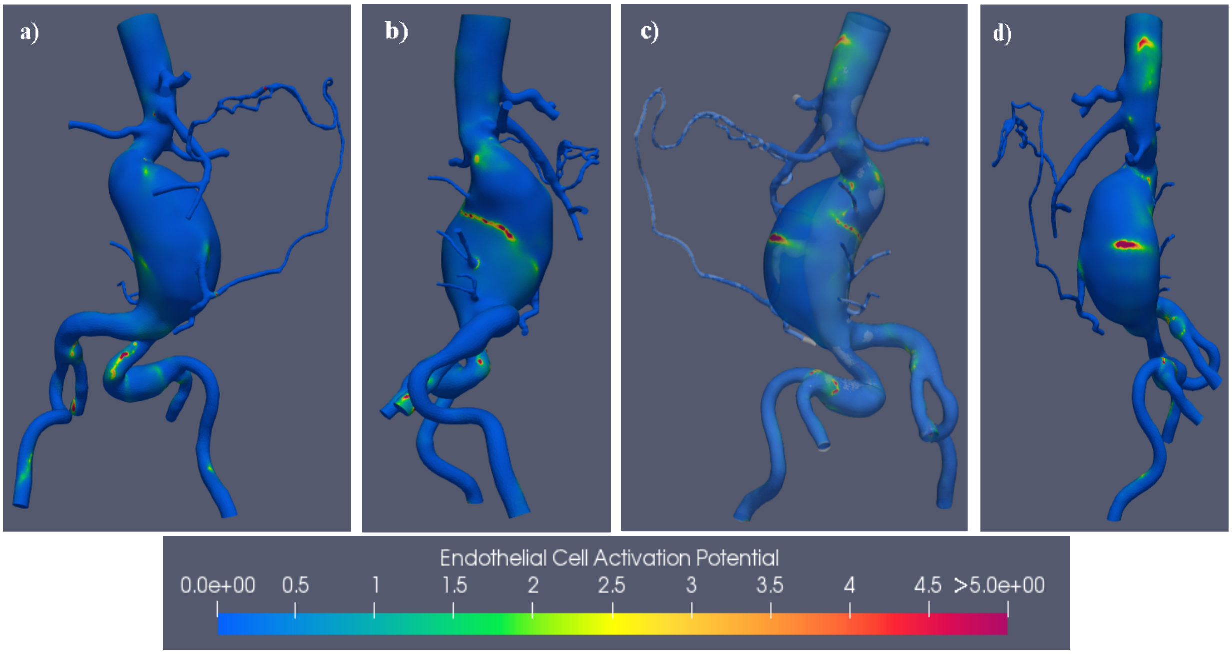

Figure 4.11: Endothelial Cell Activation Potential in the aneurysm wall geometry. a) Anterior view. b) Left lateral view. c) Posterior view. d) Right lateral view.

4.12.6 Point-Wise Residence Time

The Point-Wise Residence Time (RT_{PW}) is shown in Fig.4.12 and 4.13 in the sagittal plane and in the plane cutting through the maximum bulge of the aneurysm. As observed in Fig.4.12.a-b, high residence time can be observed predominantly inside the intraluminal thrombus (ILT) region between the aneurysm wall and lumen surfaces, outside the lumen. However, as seen in Fig.4.13.a-b, the residence time values inside the lumen geometry is reduced compared to the values observed in the aneurysm wall geometry. This is because of the increased momentum of the blood flow due to reduced size of the lumen. However, proximal to the ILT, high RT_{PW} can be observed.

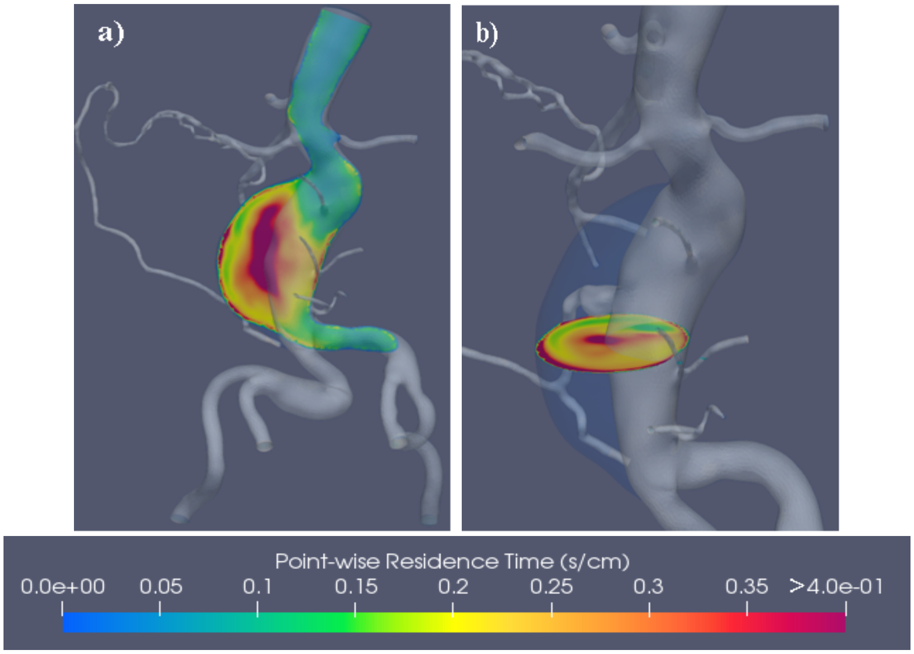

Figure 4.12: Point-Wise Residence Time in the aneurysm wall geometry. a) Sagittal plane approximately splitting aneurysm into left and right halves. b) Section through maximum bulge of the aneurysm.

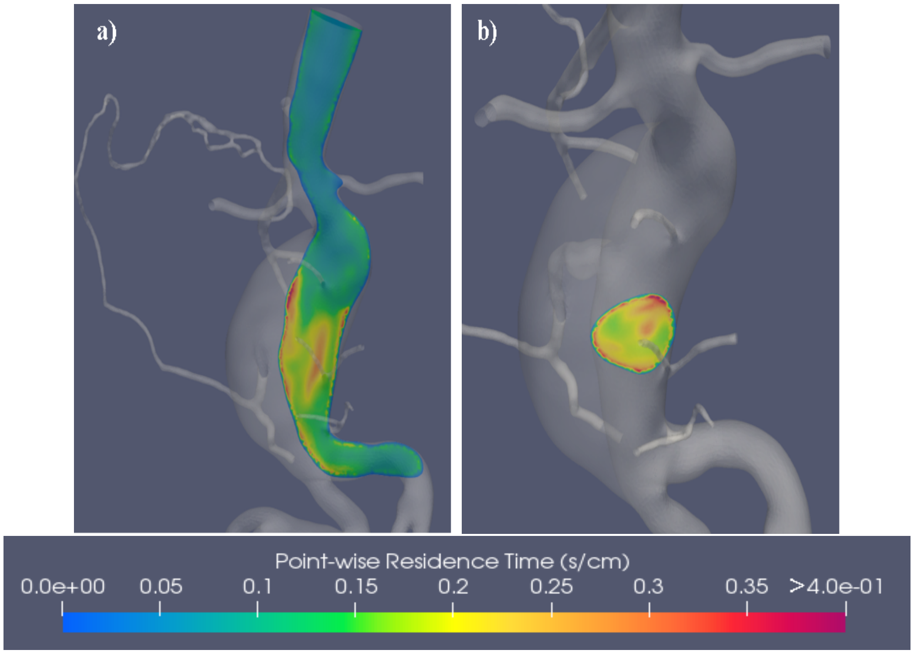

Figure 4.13: Point-Wise Residence Time in the lumen geometry. a) Sagittal plane approximately splitting aneurysm into left and right halves. b) Section through maximum bulge of the aneurysm.

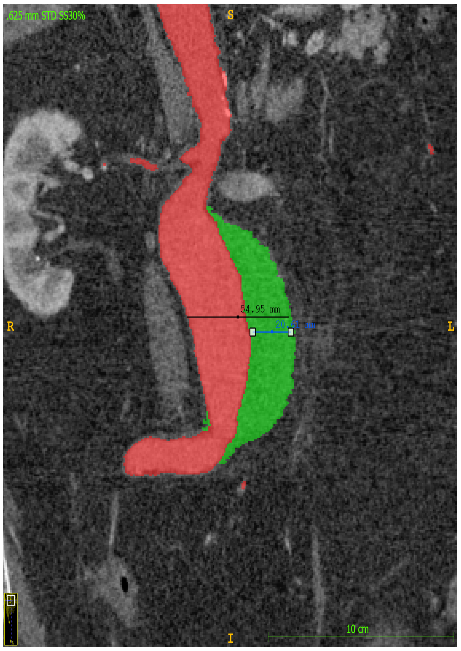

Figure 4.14: Sagittal slice through the patient's aneurysm. The lumen (red) and the intraluminal thrombus (green) is shown. The maximum diameter of the aneurysm is measured to be 5.5 cm and the thrombus thickness is measured to be 2 cm.

4.13 Discussion

In this patient, significant intraluminal thrombus deposition (2.2 cm thickness) is observed in the anterior region of the aneurysm as shown in Fig. 4.14. Les et al. (2010) suggested that the regions of low TAWSS and high OSI is associated with thrombus growth. This refers to the regions where the endothelial cells in the aneurysm wall are most susceptible. From Fig.4.11, we can observe peak values of ECAP on the anterior wall, which can be the location of thrombus initiation. Also, from Fig.4.12, high residence time in the space between the lumen and aneurysm wall surface, implies a potential region where activated platelets reside inside the aneurysm volume. Hence, when the activated platelets comes in contact with susceptible endothelial regions in the anterior wall of the aneurysm, this can lead to the initiation and deposition of thrombus. Furthermore, relatively lower values of

RT_{PW} observed inside the lumen region can lead to suppression of thrombus deposition. But, as seen from 4.13.b, high values of RT_{PW} is observed proximal to the ILT, which implies a possibility for further thrombus growth.

4.14 Conclusions

Numerical simulation of flow through lumen and wall has been studied. The flow field at different times in the cardiac cycle has been studied using 3D streamlines. The various hemodynamic metrics such as TAWSS, OSI, ECAP and RT_{PW} has been quantified and the reason for thrombus formation and deposition in the aneurysm wall geometry has been explored.

4.15 Future Research

Direct Numerical Simulation needs to be carried out to capture the transitional nature of blood flow within an aneurysm. Further, a stent-graft is to be inserted inside the aneurysm geometry to study the phenomenon of Type II endoleaks.

Bibliography

[1] Arzani, A., Les, A. S., Dalman, R. L. & Shadden, S. C. Effect of exercise on patient specific abdominal aortic aneurysm flow topology and mixing. *International Journal for Numerical Methods in Biomedical Engineering* **30**, 280–295 (2014).

[2] Arzani, A. Accounting for residence-time in blood rheology models: do we really need non-Newtonian blood flow modelling in large arteries? *Journal of The Royal Society Interface* **15**, 20180486 (2018).

[3] Di Achille, P., Tellides, G., Figueroa, C. A. & Humphrey, J. D. A haemodynamic predictor of intraluminal thrombus formation in abdominal aortic aneurysms. *Proceedings of the Royal Society A: Mathematical, Physical and Engineering Sciences* **470**, 20140163 (2014).

[4] Di Achille, P., Tellides, G. & Humphrey, J. D. Hemodynamics-driven deposition of intraluminal thrombus in abdominal aortic aneurysms. 33, (2017). *International Journal for Numerical Methods in Biomedical Engineering* **33**, e2828 (2017).

[5] Lan, H., Updegrove, A., Wilson, N., Maher, G., Shadden, S. & Marsden, A. A Re-Engineered Software Interface and Workflow for the Open-Source SimVascular Cardiovascular Modeling Package. *Journal of Biomechanical Engineering* **140**, 024501 (2018).

[6] Les, A., Yeung, J., Schultz, G., Herfkens, R., Dalman, R. & Taylor, C. Supraceliac and Infrarenal Aortic Flow in Patients with Abdominal Aortic Aneurysms: Mean Flows, Waveforms, and Allometric Scaling Relationships. *Cardiovascular Engineering and Technology* **1**, 39–51 (2010).

[7] Les, A., Shadden, S., Figueroa, C., Park, J., Tedesco, M., Herfkens, R., Dalman, R., & Taylor, C. Quantification of hemodynamics in abdominal aortic aneurysms during rest and exercise using magnetic resonance imaging and computational fluid dynamics. *Annals of Biomedical Engineering* **38**, 1288–1313 (2010).

[8] Reza, M. M. S. & Arzani, A. A critical comparison of different residence time measures in aneurysms. *Journal of Biomechanics* **88**, 122–129 (2019).

[9] Stergiopulos, N., Meister, J.-J. & Westerhof- , N. Simple and Accurate Way for Estimating Total and Segmental Arterial Compliance: The Pulse Pressure Method. *Annals of Biomedical Engineering* **22**, 392–397 (1994).